Lagrange-Remap strategy for multi-material fluid-solid simulations using compressive limiters

S. Guisset[1,2], L. Tallois[1], A. Colaïtis[3], J. Breil[1]

Abstract

In the present work, the Lagrange-Remap strategy proposed in [21] is extended to multi-material fluid-solid simulations. Both hypo-elastic and hyper-elastic material models are considered to describe the mechanical behavior of the solids. In practice, the deviatoric stress tensor (for hypo-elastic materials) and the left Cauchy-Green tensor (for isotropic hyper-elastic materials) are remapped, while the use of compressive limiters effectively reduces numerical diffusion during the remapping step. The simplicity of this diffuse interface approach is emphasized in the context of multi-material fluid-solid simulations. A series of Lagrange-Remap test cases, involving both solids and fluids, are conducted and compared with reference Lagrangian simulations, demonstrating the robustness and accuracy of the overall numerical strategy.

Key words: Hypo-elastic and hyper-elastic materials, multi-material simulations, diffuse interface methods, compressive limiters, Lagrange-Remap schemes.

1 Introduction

The simulation of the dynamic behavior of materials is of considerable interest in both natural phenomena and industrial applications. Historically, the dynamics of solids have been primarily modeled using the Finite Element Method (FEM). However, since the pioneering contributions of Wilkins [44] and Godunov [18], Finite Volume Lagrangian schemes have also been developed for solid dynamics. The updated Lagrangian framework is particularly well-suited for the simulation of deformable solids, as the computational mesh moves with the material and allows the natural tracking of free-surface boundaries as well as the multi-material interfaces. Two main approaches are commonly found in the literature to describe the behavior of elastic materials under large deformations: the hypoelastic and hyperelastic models.

[1]CEA/CESTA, 15 Avenue des Sablières CS 60001, 33116 Le Barp cedex, France
[2]Corresponding author: sebastien.guisset@cea.fr
[3]Laboratory for Laser Energetics, 250 East River Rd, Rochester, NY 14623-1212

The hypoelastic framework, introduced by Wilkins [44], formulates an additional evolution equation for the deviatoric (spherical) part of the Cauchy stress tensor, while the volumetric response, corresponding to the hydrodynamic pressure, is determined through an equation of state. The additional evolution equation must employ a non-standard derivative operator of the deviatoric stress tensor in order to guarantee the property of frame indifference. This requirement, also referred to as objectivity in the literature, ensures that the material response is independent of the chosen frame of reference. In practice, this means that the physical behavior of the solid remains unaffected by rigid body motions. The hypoelastic approach is known to present several drawbacks. First, the choice of the objective stress rate is not unique. In practice, the Jaumann rate is often adopted, but alternative formulations (e.g., Green-Naghdi or Truesdell rates) can also be used, and this choice may affect the computed evolution of the deviatoric stress tensor. Moreover, a fundamental limitation of hypoelastic models is that they may generate entropy even in reversible processes, which contradicts the principles of thermodynamics. Despite its known drawbacks, the hypoelastic approach remains widely used in practice. In particular, several works [8, 26, 37] have proposed solving the hypoelastic model within the framework of cell-centered Finite Volume Lagrangian schemes, which naturally accommodate the treatment of large deformations and multi-material interactions.

The hyperelastic approach was proposed in [18] and naturally ensures the frame-indifference and the thermodynamic consistency by construction. Here the Cauchy stress tensor is defined as the derivative of the free energy with respect to the deformation and is not subject to the theoretical drawbacks of the hypoelastic model. In [25], it is proposed to extend the GLACE scheme to the hyperelasticity system at first order in two-dimensions. The hyperelastic approach inherently satisfies both frame-indifference and thermodynamic consistency [22]. In this framework, the Cauchy stress tensor is derived directly from the material's free energy as a function of the deformation, thereby avoiding the theoretical limitations associated with the hypoelastic model. Extensions of cell-centered Lagrangian schemes to hyperelastic materials have been proposed, for instance in [6], in which the work presented in [25] is extended to the three-dimensional EUCCLHYD scheme.

The present study addresses both hypoelastic and hyperelastic models within the context of multi-material fluid-solid simulations. Such multi-material configurations are ubiquitous in nature or engineering applications and pose significant computational challenges. Over the past decades, the numerical simulation of material interfaces has been the subject of extensive research, leading to the development of various strategies. Two main approaches have emerged. The first, commonly referred to in the literature as sharp interface methods, treats materials as being immiscible, and

separated by an interface. The second category, known as diffuse interface methods, allows artificial mixing between materials within transition zones, so that interfaces are represented as smeared regions. This latter approach has gained significant popularity in recent years. This growing popularity can be explained by the fact that, since material interfaces are allowed to spread over a finite width, many of the geometrical complexities associated with sharp interface tracking are alleviated. Furthermore, the development of efficient anti-diffusive techniques, combined with the steady increase in computational power, has significantly reduced the natural numerical smearing inherent to diffuse interface approaches. For a comprehensive overview of diffuse interface strategies, we refer the reader to [38, 28] and the references therein.

In the present work, material interfaces are considered as diffuse regions where different materials may artificially mix. To limit excessive numerical diffusion during the remapping of material volume fractions, a compressive limiter is employed. This choice is motivated by the simplicity of the approach. It should be emphasized, however, that although compressive limiters significantly reduce interface smearing, the results obtained on coarse meshes remain diffused. Moreover, for any level of mesh refinement, interface reconstruction methods based on geometrical approaches remain more accurate than diffuse interface techniques. The diffuse interface strategy is therefore adopted here as a compromise, offering a balance between accuracy through the mitigation of numerical diffusion and simplicity relative to the complexity of interface reconstruction methods [4]. Concerning the treatment of the mixed cells, the equal strain closure is adopted here. It assumes that the material volumic fractions stay constant during the Lagrangian phase. In this case, it is supposed that all materials are compressed or expanded with the same rate. The main advantage of this closure lies in its numerical simplicity, while still providing sufficiently accurate results for a wide range of multiphase applications [4]. Nevertheless, this assumption has important limitations: when dealing with materials governed by highly contrasted equations of state (e.g., air and water), a strong non-physical pressure decoupling may occur within mixed cells. A detailed analysis of this issue is provided in [30].

On the numerical side, the strategy adopted in this work belongs to the class of "Lagrangian plus Remapping" methods, also referred to as indirect Euler approaches. In this framework, the explicit Lagrangian phase is first solved, during which the computational mesh moves with the fluid or solid velocity. This formulation is particularly well suited for multi-material simulations, as material interfaces are followed exactly. However, when strong deformations occur, the mesh quality can quickly deteriorate, potentially leading to mesh tangling. To overcome this difficulty, the solution is remapped at the end of each Lagrangian step onto the initial mesh. This last stage is critical when working with multi-material flows and must be

carefully addressed. Overall, the Lagrangian plus Remapping approach has proven highly effective for multiphase flow simulations and has gained wide popularity in the community [4, 2, 14].

We do not aim to review the numerous numerical methods developed for Lagrangian hydrodynamics in this introduction, as comprehensive surveys can easily be found in the literature. In this work, we adopt a cell-centered Lagrangian finite volume scheme. This class of methods, rooted in the pioneering work of Godunov [19], relies on cell-centered quantities. The nodal velocities are obtained through a nodal solver, and several multidimensional extensions have been proposed over the years [13, 27]. The multi-material remapping step employed here is based on a sweeping technique. Originally introduced in [31], this approach has become popular because it avoids the costly computation of intersections between meshes (exact remapping). Conceptually, the method can be viewed as a compatibility exercise: the volume integral of a new cell is obtained from the volume integral of the old cell, augmented by the contributions of the regions swept by the displacement of the cell faces. In addition, the remapping procedure adopted in this work considers the remapping of the material internal energies. This step is delicate, as a straightforward remapping does not guarantee discrete conservation of the total energy. To address this issue, the total kinetic energy is also remapped and subsequently used to correct the material internal energies. More precisely, we employ the correction strategy proposed in [12], which ensures discrete total energy conservation. Furthermore, it can be shown that the resulting corrections to the material internal energies remain positive, thereby preserving thermodynamic consistency.

Several related contributions can be found in the scientific literature on this topic. In particular, in [9] interface-aware subscale closure model was proposed together with a multi-material remapping strategy for simulating compressible hydrodynamic problems within the cell-centered Lagrange-Remap framework. The Volume of Fluid method is employed to capture material interfaces, and a range of multi-material problems, including both gas and solid dynamics, are considered. In addition, in [15], a Lagrange-Remap method was proposed for interface flows with an arbitrary number of compressible components. Their approach extends the classical two-material five-equation model to a multi-component framework. In order to mitigate the excessive numerical diffusion of material interfaces, an anti-dissipative projection step is presented. In [43], the remapping stage of the Lagrange-Remap method is reformulated to improve computational efficiency while retaining robustness for multimaterial flow simulations.

In the present work, the Lagrange-Remap strategy introduced in [21] is extended to the context of multi-material fluid-solid simulations. More precisely, both hypo-elastic and hyper-elastic constitutive models are incorporated to describe the mechanical response of solids. A particular attention is devoted to the remapping stage, which plays a critical role in the

accuracy of such approaches. In this context, compressive limiters are introduced to reduce numerical diffusion at material interfaces. While these techniques are widely used in fluid dynamics, their application to coupled fluid-solid configurations remains uncommon and is assessed in the present study. A remapping of the variables associated with solid behavior is performed, including the deviatoric stress tensor in the hypoelastic case and the left Cauchy-Green tensor in the hyperelastic case. Special care is taken in the projection of energy variables to ensure discrete total energy conservation during the remapping step. Furthermore, systematic numerical comparisons are carried out against reference Lagrangian simulations, providing a consistent validation of the proposed methodology.

The document is organized as follows. Section 2 introduces the governing equations for solid mechanics together with their extension to multi-material configurations. Section 3 presents the multi-material Lagrangian scheme, with particular emphasis on the discretization of the material internal energy formulation. Section 4 discusses the multi-material remapping procedure, including the sweeping algorithm and the use of compressive limiters to mitigate numerical diffusion. Finally, Section 5 reports several fluid-solid test cases that are performed to evaluate the accuracy and robustness of the proposed numerical strategy.

2 Governing equations

The behavior of an elastic material can be described by a system of conservation laws, formulated in terms of the Euler equations coupled with a Cauchy stress tensor $\mathbb{T}$ [29]. The stress tensor $\mathbb{T}$ is symmetric, i.e., $\mathbb{T} = \mathbb{T}^t$, where the index t denotes the matrix transposition. Let ρ denote the mass density of the solid, $\boldsymbol{V}$ its velocity vector, and E its specific total energy. In the updated Lagrangian framework, the governing system of equations takes the form

$$\begin{aligned} \rho \frac{d}{dt}\left(\frac{1}{\rho}\right) &= \nabla \cdot \boldsymbol{V}, \\ \rho \frac{d}{dt}\boldsymbol{V} &= -\nabla \cdot \mathbb{T}, \\ \rho \frac{d}{dt}E &= -\nabla \cdot (\mathbb{T}\boldsymbol{V}), \end{aligned}$$

with the material time derivative notation

$$\frac{d}{dt}(\cdot) = \frac{\partial}{\partial t}(\cdot) + \boldsymbol{V} \cdot \nabla(\cdot).$$

The governing equations correspond respectively to the conservation of mass, momentum, and specific total energy. The specific internal energy ε is given

by

$$\varepsilon = E - \frac{1}{2}\boldsymbol{V}\cdot\boldsymbol{V}.$$

The trajectory equation which provides the position of a point of the domain with respect to time writes

$$\begin{cases} \dfrac{d\boldsymbol{x}}{dt} = \boldsymbol{V}, \\ \boldsymbol{x}(t=0) = \boldsymbol{X}. \end{cases}$$

In this equation, $\boldsymbol{X}$ is the position of point $\boldsymbol{x}(t)$ at initial time $t = 0$. Finally, to close the system, constitutive relations must be provided to relate the thermodynamic variables to the Cauchy stress tensor $\mathbb{T}$. These relations need to be specified.

Pure hydrodynamics model

In the case of a pure hydrodynamic model, the Cauchy stress tensor simply reduces to its hydrostatic component, represented by the pressure p. Specifically, the stress tensor takes the form

$$\mathbb{T} = -p\,\mathrm{Id},$$

where Id denotes the identity tensor and p is the hydrodynamic pressure. In the present work, the fluids used in the numerical tests section are restricted to the ideal (perfect) gas regime. The associated equation of state is given by

$$p = (\gamma - 1)\,\rho\varepsilon,$$

where $\gamma > 1$ is the polytropic index of the gas. The corresponding speed of sound a writes

$$a^2 = \gamma\frac{p}{\rho}.$$

Hypo-elasticity model

In the context of a hypo-elastic modeling of elastic materials, the Cauchy stress tensor $\mathbb{T}$ is decomposed into a hydrostatic and a deviatoric components

$$\mathbb{T} = -p\,\mathrm{Id} + \mathbb{S},$$

where p denotes the hydrodynamic pressure and $\mathbb{S}$ represents the deviatoric (traceless) part of the stress tensor. The equation of state governing the hydrostatic component is specified by relating the pressure to the density and the specific internal energy

$$p = p(\rho, \varepsilon).$$

The evolution of the deviatoric stress tensor $\mathbb{S}$ for an elastic, perfectly plastic material is governed by an incremental constitutive law. To formulate this

evolution equation, the strain-rate tensor $\mathbb{D}$ is introduced. It is defined as the symmetric part of the velocity gradient

$$\mathbb{D} = \frac{1}{2}\left(\nabla \boldsymbol{V} + (\nabla \boldsymbol{V})^T\right).$$

The time evolution of $\mathbb{S}$ is governed by a Wilkins-type constitutive relation [44]

$$\frac{d\mathbb{S}}{dt} = 2\mu\left(\mathbb{D}_0 - \mathbb{D}_p\right) - \left(\mathbb{S}\mathbb{W} - \mathbb{W}\mathbb{S}\right), \tag{1}$$

where μ is known as the shear modulus, $\mathbb{D}_0$ is the deviatoric part of the strain-rate tensor, and $\mathbb{D}_p$ represents the plastic part of the strain rate. The deviatoric strain rate is defined as

$$\mathbb{D}_0 = \mathbb{D} - \frac{1}{3}\operatorname{tr}(\mathbb{D})\,\mathrm{Id},$$

where $\operatorname{tr}(\cdot)$ denotes the trace operator. The antisymmetric part of the velocity gradient, known as the spin tensor, is defined by

$$\mathbb{W} = \frac{1}{2}\left(\nabla \boldsymbol{V} - (\nabla \boldsymbol{V})^T\right).$$

The combination of the time derivative and the rotational terms in equation (1) constitutes the Jaumann derivative, which ensures objectivity [22]. The plastic behavior is constrained by the von Mises yield criterion and expressed thanks to the yield function

$$f^{\text{yield}} = \sqrt{\mathbb{S} : \mathbb{S}} - \sqrt{\frac{2}{3}} Y_0 \leq 0,$$

where Y_0 denotes the yield strength of the material, assumed constant for perfectly plastic behavior. The plastic strain rate is expressed as

$$\mathbb{D}_p = \chi\left(\mathbb{N}_p : \mathbb{D}\right)\mathbb{N}_p, \tag{2}$$

where

$$\mathbb{N}_p = \frac{\mathbb{S}}{\sqrt{\mathbb{S} : \mathbb{S}}},$$

denotes the plastic flow direction [22]. Throughout this work, it is assumed that $\mathbb{S} \neq 0$ whenever the plastic flow direction $\mathbb{N}_p$ is defined. In equation (2), the parameter χ acts as a switching function that governs the onset of plastic deformation and is defined as

$$\chi = \begin{cases} 0 & \text{if } \left(f^{\text{yield}} < 0\right) \text{ or if } \left(f^{\text{yield}} = 0 \text{ and } (\mathbb{N}_p : \mathbb{B}) \leq 0\right), \\ 1 & \text{if } \left(f^{\text{yield}} = 0\right) \text{ and } (\mathbb{N}_p : \mathbb{B}) > 0. \end{cases}$$

For more details on plasticity aspects we refer to [26, 39]. In the numerical tests section, the behavior of the materials used follow a Mie-Grüneisen equation of state. In this case, for a given specific internal energy ε and specific volume $V = 1/\rho$, the pressure is expressed as

$$p(V,\varepsilon) = \frac{a_0^2(V_0 - V)}{[V_0 - s(V_0 - V)]^2} + \frac{\Gamma(V)}{V}\left[\varepsilon - \frac{1}{2}\left(\frac{a_0(V_0 - V)}{V_0 - s(V_0 - V)}\right)^2\right],$$

where $V_0 = 1/\rho_0$ is the specific volume of the unstressed material. The parameters a_0 and s are material constants and define the empirical linear relation between the shock velocity U_s and the particle velocity u_p as $U_s = a_0 + su_p$ [32]. The Grüneisen parameter $\Gamma(V)$ is defined as

$$\Gamma(V) = V\left(\frac{\partial p}{\partial \varepsilon}\right)_V = \Gamma_0 \frac{V}{V_0},$$

where Γ_0 denotes the Grüneisen parameter at reference conditions

$$\Gamma_0 = V_0\left(\frac{\partial p}{\partial \varepsilon}\right)_{V=V_0}.$$

The second equality is an empirical relation that assumes the Grüneisen parameter varies linearly with the specific volume [40]. Following [26], in order to ease the numerical implementation the equation of state is recast in terms of the density and internal energy

$$p(\rho,\varepsilon) = \rho_0 a_0^2 f(\eta) + \rho_0 \Gamma_0 \varepsilon,$$

with the dimensionless compression ratio $\eta = \rho/\rho_0$ and

$$f(\eta) = \frac{(\eta - 1)[\eta - \Gamma_0(\Gamma - 1)/2]}{(\eta - s(\eta - 1))^2}.$$

For a general equation of state of the form $p = p(\rho,\varepsilon)$, the isentropic sound speed a is defined by

$$a^2 = \left(\frac{\partial p}{\partial \rho}\right)_\varepsilon + \frac{p}{\rho^2}\left(\frac{\partial p}{\partial \varepsilon}\right)_\rho.$$

Applying this to the Mie-Grüneisen equation of state yields

$$a^2 = a_0^2 f'(\eta) + \frac{\Gamma_0}{\rho_0}\frac{p}{\eta^2}, \quad \text{with} \quad f'(\eta) = \frac{\eta + (s - \Gamma_0)(\eta - 1)}{(\eta - s(\eta - 1))^3}.$$

Finally, the longitudinal sound speed is defined as

$$(a^L)^2 = a^2 + \frac{4}{3}(a^T)^2,$$

where the transverse sound speed is given by

$$(a^T)^2 = \frac{\mu}{\rho},$$

with μ denoting the shear modulus of the material.

Hyper-elasticity model (case of isotropic materials)
In the case of a modeling of isotropic hyper-elastic materials, the system of conservation laws is augmented by a geometrical evolution equation that governs the time evolution of the left Cauchy-Green deformation tensor denoted $\mathbb{B}$. This tensor is defined as

$$\mathbb{B} = \mathbb{F}\mathbb{F}^T,$$

where $\mathbb{F}$ is the deformation gradient. The evolution of $\mathbb{B}$ is given by the following equation [29, 23, 42]

$$\frac{d\mathbb{B}}{dt} = (\nabla \boldsymbol{V})\,\mathbb{B} + \mathbb{B}\,(\nabla \boldsymbol{V})^T.$$

In order to close the system of equations, a constitutive relation must be introduced to relate the thermodynamic variables to the Cauchy stress tensor $\mathbb{T}$. According to the representation theorem [42], the free energy can be expressed as a scalar function of the three principal invariants of the tensor $\mathbb{B}$ as well as the temperature

$$\psi = \psi\left(i_1(\mathbb{B}),\, i_2(\mathbb{B}),\, i_3(\mathbb{B}),\, \theta\right),$$

where θ denotes the temperature and the invariants of $\mathbb{B}$ are given by

$$\begin{cases} i_1(\mathbb{B}) = \mathrm{tr}(\mathbb{B}), \\ i_2(\mathbb{B}) = \dfrac{1}{2}\left[\mathrm{tr}(\mathbb{B})^2 - \mathrm{tr}(\mathbb{B}^2)\right], \\ i_3(\mathbb{B}) = \det(\mathbb{B}). \end{cases}$$

It is assumed that the free energy ψ can be decomposed additively into a volumetric and a isochoric (shear) contribution [23]

$$\psi\left(J, \bar{\mathbb{B}}, \theta\right) = \psi_v\left(J, \theta\right) + \psi_s\left(i_1(\bar{\mathbb{B}}), i_2(\bar{\mathbb{B}}), \theta\right),$$

where $J = \sqrt{\det(\mathbb{B})}$ denotes the Jacobian determinant of the deformation gradient and $\bar{\mathbb{B}} = J^{-2/3}\mathbb{B}$ is the isochoric part of the left Cauchy-Green tensor $\mathbb{B}$. The invariants of the normalized tensor $\bar{\mathbb{B}}$ are related to those of $\mathbb{B}$ as follows

$$\begin{cases} i_1(\bar{\mathbb{B}}) = J^{-2/3}\, i_1(\mathbb{B}), \\ i_2(\bar{\mathbb{B}}) = J^{-2/3}\, i_2(\mathbb{B}), \\ i_3(\bar{\mathbb{B}}) = 1. \end{cases}$$

Finally, the Cauchy stress tensor $\mathbb{T}$ is computed from the free energy through the relation [33]

$$\mathbb{T} = 2\rho \left(\frac{\partial \psi}{\partial \bar{\mathbb{B}}} \right)_\theta \bar{\mathbb{B}},$$

which, upon substituting the additive energy decomposition, leads to the expression [33]

$$\mathbb{T} = \rho J \left(\frac{\partial \psi_v}{\partial J} \right)_\theta \mathrm{Id} + 2\rho \left[\left(\frac{\partial \psi_s}{\partial i_1(\bar{\mathbb{B}})} \right)_\theta \bar{\mathbb{B}}_0 - \left(\frac{\partial \psi_s}{\partial i_2(\bar{\mathbb{B}})} \right)_\theta \left(\bar{\mathbb{B}}^{-1} \right)_0 \right],$$

where $\bar{\mathbb{B}}_0$ denotes the deviatoric part of $\bar{\mathbb{B}}$, defined as

$$\bar{\mathbb{B}}_0 = \bar{\mathbb{B}} - \frac{1}{3} \mathrm{tr}(\bar{\mathbb{B}}) \mathrm{Id}.$$

The Cauchy stress tensor can finally be decomposed into its hydrostatic and deviatoric components

$$p(J, \theta) = -\rho J \left(\frac{\partial \psi_v}{\partial J} \right)_\theta = -\rho^2 \left(\frac{\partial \psi_v}{\partial \rho} \right)_\theta,$$

$$\mathbb{S}(i_1(\bar{\mathbb{B}}), i_2(\bar{\mathbb{B}}), \theta) = 2\rho \left[\left(\frac{\partial \psi_s}{\partial i_1(\bar{\mathbb{B}})} \right)_\theta \bar{\mathbb{B}}_0 - \left(\frac{\partial \psi_s}{\partial i_2(\bar{\mathbb{B}})} \right)_\theta \left(\bar{\mathbb{B}}^{-1} \right)_0 \right].$$

In the present document a compressible Neo-Hookean model is selected. This model is one of the simplest yet effective models for hyperelastic solids. In this case, the free energy is defined by

$$\psi_v(J, \eta) = \frac{\kappa}{4J\rho} \left[(J-1)^2 + (\log J)^2 \right],$$
$$\psi_s(i_1(\bar{\mathbb{B}}), \eta) = \frac{\mu}{2J\rho} \left[i_1(\bar{\mathbb{B}}) - 3 \right],$$

where μ and λ are the Lamé coefficients, and $\kappa = \lambda + \frac{2}{3}\mu$ is the bulk modulus. Computing the derivative of the above expressions yields the following form for the pressure and deviatoric stress

$$p = -\frac{\kappa}{2} \left[(J-1) + \frac{\log(J)}{J} \right], \qquad \mathbb{S} = \frac{\mu}{J} \left(\bar{\mathbb{B}} - \frac{1}{3} \mathrm{tr}(\bar{\mathbb{B}}) \mathrm{Id} \right).$$

Finally, the mechanical properties of materials are often characterized by the Young modulus E, the Poisson ratio ν, and the shear modulus μ (also referred to as the second Lamé coefficient). These parameters are related through the following expressions

$$\mu = \frac{E}{2(1+\nu)}, \qquad \lambda = \frac{E\nu}{(1+\nu)(1-2\nu)},$$

where λ denotes the first Lamé coefficient. The longitudinal sound speed is defined as

$$(a^L)^2 = a^2 + \frac{4}{3}(a^T)^2,$$

where the bulk (acoustic) and the transverse sound speeds are defined by

$$(a)^2 = \frac{\kappa}{\rho}, \qquad (a^T)^2 = \frac{\mu}{\rho}.$$

Multi-material aspects

A mixture made of an arbitrary number of materials is considered. The volume fraction of material k is denoted by α^k and its density by ρ^k. Inside a given volume V where a mass m^k of material k occupies a volume V^k, these quantities are defined as follows

$$\alpha^k = \frac{V^k}{V}, \qquad \rho^k = \frac{m^k}{V^k}.$$

The total density of the mixture denoted ρ is defined as

$$\rho = \frac{m}{V} = \sum_k \alpha^k \rho^k.$$

Similarly, specific internal energy of material k is denoted ε^k. Likewise, a specific internal energy for the mixture denoted ε is defined as

$$m\varepsilon = \sum_k m^k \varepsilon^k.$$

Each material k has its own pressure p^k, Cauchy tensor $\mathbb{T}^k$ and entropy η^k. The quantities ρ^k, ε^k and p^k are related to each other through an equation of state $p^k(\rho^k, \varepsilon^k)$. Finally, the characteristic times at which material velocities relax to a common value are assumed to be significantly smaller than the characteristic times of observation such that all materials share the same velocity.

Equal strain assumption model

In the following, the so-called *equal strain assumption* [4] is studied. Here, all constituent materials are assumed to undergo the same volume deformation. Therefore, under this assumption the volume fractions α^k of the materials are constant in time

$$\frac{d}{dt}\left(\alpha^k\right) = 0.$$

The material density evolution equation writes

$$\alpha^k \rho^k \frac{d}{dt}\left(\frac{1}{\rho^k}\right) = \alpha^k \nabla \cdot \boldsymbol{V},$$

and the internal energy evolution equation for each material k reads

$$\alpha^k \rho^k \frac{d}{dt}\varepsilon^k = -\alpha^k \mathbb{T}^k : \nabla \boldsymbol{V}.$$

The total pressure and Cauchy stress tensor of the mixture are defined as

$$p = \sum_k \alpha^k p^k, \qquad \mathbb{T} = \sum_k \alpha^k \mathbb{T}^k.$$

This formulation leads to a hyperbolic system, where the speed of sound a in the mixture is expressed as

$$a^2 = \sum_k \frac{m^k}{m}(a^k)^2 = (a^L)^2 + (a^T)^2 = \sum_k \frac{m^k}{m}(a^{k,L})^2 + \sum_k \frac{m^k}{m}(a^{k,T})^2,$$

where

$$(a^k)^2 = (a^{k,L})^2 + (a^{k,T})^2.$$

Here, a^L and a^T denote the longitudinal and transverse sound speeds of the mixture, respectively, while $a^{k,L}$ and $a^{k,T}$ correspond to the longitudinal and transverse sound speeds of material k. This model is widely used for the simulation of multi-material flows [5]. However, it is noticed that while this closure is well-suited for mixtures of similar materials, it may become inaccurate when the constituents possess significantly different equations of state. This limitation is discussed in [30], where an alternative equal-pressure model is proposed. In practice, the procedure to compute the new material internal energies is as follows: first, the total energy evolution equation is solved. At this point, the total internal energy equation can be deduced by removing the kinetic energy part (computed from the momentum equation). Secondly, the total entropy dissipation is computed and distributed according to the volume fraction of each material as follows

$$m^k \left(Td\eta\right)^k = \alpha^k m \left(Td\eta\right), \;\; \Leftrightarrow \;\; \rho^k \left(Td\eta\right)^k = \rho \left(Td\eta\right).$$

This yields the following relation for the internal energy evolution of each material

$$\alpha^k \rho^k \frac{d}{dt}\varepsilon^k - \alpha^k \mathbb{T}^k : \nabla \boldsymbol{V} = \alpha^k \left(\rho \frac{d}{dt}\varepsilon - \mathbb{T} : \nabla \boldsymbol{V}\right).$$

The above relation plays a central role in the next sections, as it is systematically employed to update the material internal energies. The corresponding numerical scheme is presented in the next section.

3 Cell-centered Lagrangian schemes

3.1 Notations

In this section, the notations introduced in [20] are adopted. The computational domain, denoted by $\omega(t)$, is discretized into a set of non-overlapping

polyhedral cells ω_c such that $\omega(t) = \bigcup_c \omega_c$. Each polyhedron represents a volume enclosed by polygonal faces. In the three-dimensional setting, these faces are not necessarily planar, making the definitions of outward normals and face areas non-trivial. Following the approach in [17], each face is subdivided by introducing an auxiliary point p_f^*, one per face. This construction enables to ensure the satisfaction of the Geometrical Conservation Law (GCL) which guaranty a discrete compatibility between mass conservation and mesh geometry. The splitting of faces introduces triangular elements denoted t_r. For completeness, we summarize the notations used throughout this section

- $\mathcal{P}(c)$ is the set of nodes p of cell c without the nodes p_f^*,
- $\mathcal{F}(c,p)$ is the set of faces f of cell c and sharing point p,
- $\mathcal{C}(p)$ is the set of cells c sharing node p,
- $\mathcal{T}(c)$ is the set of all the triangles t_r resulting from the splitting of the faces of cell c,
- $\mathcal{T}(c,f)$ is the set of triangles t_r resulting from the splitting of the face f of cell c,
- $\mathcal{T}(c,f,p)$ is the set of triangles t_r resulting from the splitting of the face f of cell c and sharing point p.

Concerning the cell variables, the approach is that of a finite volume scheme. For material physical quantities $\phi^k \in \left\{1/(\alpha^k\rho^k), 1/\rho^k, \varepsilon^k\right\}$ related to a material k and a cell c, one defines the averaged quantities over the cell by

$$m_c^k = \int_{\omega_c} \alpha^k\rho^k dv, \qquad \phi_c^k = \frac{1}{m_c^k}\int_{\omega_c} \alpha^k\rho^k\phi dv,$$
$$m_c = \int_{\omega_c} \rho dv, \qquad \boldsymbol{V}_c = \frac{1}{m_c}\int_{\omega_c} \rho\boldsymbol{V} dv, \qquad E_c = \frac{1}{m_c}\int_{\omega_c} \rho E dv.$$

Defining these averaged quantities prepares for the use of Reynold's transport theorem which is used extensively in the next section.

3.2 Numerical schemes

In this section the semi-discrete multi-material Lagrangian scheme is presented. In particular, the evolution equation to update the material internal energy equations is detailed.

3.2.1 Momentum and total energy equation

The numerical scheme used for the Lagrangian step is taken from [17]. Recall that in a Lagrangian framework, the mass inside a cell is constant, i.e., the cell mass m_c remains constant. In this setting, the semi-discrete momentum and total energy conservation equations writes

$$\begin{aligned} m_c \frac{d\boldsymbol{V}_c}{dt} + \sum_{p\in\mathcal{P}(c)} \sum_{f\in\mathcal{F}(c,p)} s_{pf} \mathbb{T}_{cfp} \boldsymbol{n}_{pf} = \boldsymbol{0}, \\ m_c \frac{dE_c}{dt} + \sum_{p\in\mathcal{P}(c)} \sum_{f\in\mathcal{F}(c,p)} s_{pf} \mathbb{T}_{cfp} \boldsymbol{V}_p \cdot \boldsymbol{n}_{pf} = 0, \end{aligned} \tag{3}$$

where the index c denotes that the quantity has been mass-averaged over the cell. Additionally, the semi-discrete trajectory equation is given by

$$\frac{d\boldsymbol{x}_p}{dt} = \boldsymbol{V}_p.$$

Solving this equation allows one to compute the updated cell volume. The nodal fluxes $\mathbb{T}_{cfp}$ and the nodal velocities $\boldsymbol{V}_p$ are the remaining unknowns to be determined. To ensure a semi-discrete positive entropy production [27], the pressure jumps are written in terms of velocity jumps as

$$\mathbb{T}_{cfp} - \mathbb{T}_c = \left[\mathbb{Q}_{cfp} \left(\boldsymbol{V}_p - \boldsymbol{V}_c\right)\right] \otimes \boldsymbol{n}_{pf},$$

where $\mathbb{Q}_{cfp}$ is a positive definite tensor. To enforce discrete momentum and total energy conservation, the nodal velocity $\boldsymbol{V}_p$ is computed by imposing a momentum balance around the node p leading to the equation

$$\mathbb{M}_p \boldsymbol{V}_p = \boldsymbol{B}_p,$$

where

$$\mathbb{M}_p = \sum_{c\in\mathcal{C}(p)} \sum_{f\in\mathcal{F}(c,p)} s_{pf} \mathbb{Q}_{cfp}, \qquad \boldsymbol{B}_p = \sum_{c\in\mathcal{C}(p)} \sum_{f\in\mathcal{F}(c,p)} s_{pf} \left[\mathbb{Q}_{cfp} \boldsymbol{V}_c - \mathbb{T}_c \boldsymbol{n}_{pf}\right],$$

and the following definition for the tensor $\mathbb{Q}_{cfp}$

$$\mathbb{Q}_{cfp} = \rho_c \left[a_c^L \left(\boldsymbol{n}_{pf} \otimes \boldsymbol{n}_{pf}\right) + a_c^T \left(\mathrm{Id} - \boldsymbol{n}_{pf} \otimes \boldsymbol{n}_{pf}\right)\right].$$

Here, a_c^L and a_c^T are the longitudinal and transverse wave speeds. Since $\mathbb{M}_p$ is positive definite, it is invertible, and the nodal velocity $\boldsymbol{V}_p$ can be determined explicitly. For completeness, we finally recall the definition of the face area vector $s_{pf}\boldsymbol{n}_{pf}$

$$s_{pf}\boldsymbol{n}_{pf} = \frac{1}{3} \left(\sum_{t_r\in\mathcal{T}(c,f,p)} s_{t_r} \boldsymbol{n}_{t_r} + \sum_{t_r\in\mathcal{T}(c,f)} \frac{1}{N_{p,f}} s_{t_r} \boldsymbol{n}_{t_r} \right),$$

and refer to [17] for its importance in enforcing the GCL condition. In this last equation, $N_{p,f}$ is the number of nodes on the face f, $\boldsymbol{n}_{t_r}$ the unit outward normal on the triangle t_r and the term $s_{pf}\boldsymbol{n}_{pf}$ is called face area vector and may be seen as the contribution of face f to the corner area vector where the corner area vector writes $\boldsymbol{n}_p = \sum_{f\in\mathcal{F}(c,p)} s_{pf}\boldsymbol{n}_{pf}$.

3.2.2 Material internal energy equations

Following the cell-centered strategy presented in [17] the GCL compatibility gives the discrete version of the operators. In particular the discrete velocity gradient writes

$$(\nabla \boldsymbol{V})_c = \frac{1}{v_c}\sum_{p\in\mathcal{P}(c)}\sum_{f\in\mathcal{F}(c,p)} s_{pf}\boldsymbol{V}_p \otimes \boldsymbol{n}_{pf}.$$

where v_c denotes the volume of cell c. Applying this discretisation to the equal stress assumption equation (2), one obtains the following scheme to update the material internal energy

$$m_c^k \frac{d\varepsilon_c^k}{dt} - \alpha_c^k \mathbb{T}_c^k : \sum_{p\in\mathcal{P}(c)}\sum_{f\in\mathcal{F}(c,p)} s_{pf}\boldsymbol{V}_p \otimes \boldsymbol{n}_{pf} = \alpha_c^k \left[m_c \frac{d\varepsilon_c}{dt} - \mathbb{T}_c : \sum_{p\in\mathcal{P}(c)}\sum_{f\in\mathcal{F}(c,p)} s_{pf}\boldsymbol{V}_p \otimes \boldsymbol{n}_{pf} \right].$$

To conclude this section, it is emphasized that, in practice, second-order extensions are employed. The approach adopted to achieve second-order spatial accuracy follows precisely the methodology presented in [17]. For time integration, a direct predictor-corrector strategy is applied.

4 Multi-material remapping aspects

In this section, a multi-material face sweeping strategy is introduced. It builds upon the 3D sweeping procedure described in [31, 20], and relies on a compressive limiter technique [41, 34, 45]. As discussed in [21], the compressive limiter enables to control the numerical diffusion of the volume fraction. Let ψ be a variable defined over a collection of non-overlapping polyhedra $\{c\}$ to be remapped onto a new collection of cells denoted by $\{\tilde{c}\}$. More precisely, given ψ defined on the original cells $\{c\}$, the goal is to compute the cell-average of ψ over $\tilde{c}$

$$\psi_{\tilde{c}} = \frac{1}{V_{\tilde{c}}}\int_{\tilde{c}} \psi \, dv,$$

where $V_{\tilde{c}}$ is the volume of the new cell $\tilde{c}$. In the context of multi-material pure hydrodynamic simulations, the following quantities must be remapped:

material masses, specific internal energies, cell volumes, and total momentum. Accordingly, we set

$$\psi \in \{\alpha^k\rho^k,\, \alpha^k,\, \alpha^k\rho^k\varepsilon^k,\, \rho\boldsymbol{V}\}.$$

In the case of hypo-elastic materials, the deviatoric stress tensor must also be remapped therefore

$$\psi \in \{\alpha^k\rho^k,\, \alpha^k,\, \alpha^k\rho^k\varepsilon^k,\, \rho\boldsymbol{V},\, \mathbb{S}^k\},$$

where $\mathbb{S}^k$ denotes the deviatoric stress tensor associated to material k. For hyper-elastic materials, the left Cauchy-Green tensor is also included

$$\psi \in \{\alpha^k\rho^k,\, \alpha^k,\, \alpha^k\rho^k\varepsilon^k,\, \rho\boldsymbol{V},\, \mathbb{B}^k\},$$

where $\mathbb{B}^k$ is the left Cauchy-Green tensor for material k. These tensors are remapped componentwise using the face-sweeping procedure. The volume $V_{\tilde{c}}$ of the new cell $\tilde{c}$ is computed from the original volume V_c and the signed volumes of the swept regions during the motion of each triangle associated with a face (triangles are obtained by splitting the cell faces). Each swept region forms a prism, denoted $\mathcal{P}_{\{p,\,p^+,\,p^{++}\}}$, where p, p^+, and p^{++} are the vertices of the triangle. The corresponding swept volume is denoted $V(\mathcal{P}_{\{p,\,p^+,\,p^{++}\}})$ and is illustrated in blue in Figure 1. The updated volume of cell $\tilde{c}$ is thus given by

$$V_{\tilde{c}} = V_c + \sum_{\{p,\,p^+,\,p^{++}\}\in\mathcal{T}(c)} V(\mathcal{P}_{\{p,\,p^+,\,p^{++}\}}).$$

The computation of the new variable $\psi_{\tilde{c}}$ is then obtained using the following relation

$$\psi_{\tilde{c}} = \frac{1}{V_{\tilde{c}}}\left(\int_c \psi\, dv + \sum_{\{p,\,p^+,\,p^{++}\}\in\mathcal{T}(c)} \int_{\mathcal{P}_{\{p,\,p^+,\,p^{++}\}}} \psi\, dv\right), \tag{4}$$

where the second term on the right-hand side accounts for the contribution of the swept regions. These integrals are evaluated using piecewise-linear reconstructions as well as a standard upwind strategy

$$\int_{\mathcal{P}_{\{p,\,p^+,\,p^{++}\}}} \psi\, dv = \begin{cases} \displaystyle\int_{\mathcal{P}_{\{p,\,p^+,\,p^{++}\}}} \psi_{c^+}(\boldsymbol{x})\, dv & \text{if} \quad V(\mathcal{P}_{\{p,\,p^+,\,p^{++}\}}) > 0, \\ \displaystyle\int_{\mathcal{P}_{\{p,\,p^+,\,p^{++}\}}} \psi_{c}(\boldsymbol{x})\, dv & \text{if} \quad V(\mathcal{P}_{\{p,\,p^+,\,p^{++}\}}) < 0, \end{cases}$$

where c and c^+ are the two neighboring cells sharing the triangle $\{p,\, p^+,\, p^{++}\}$, and $\psi_c(\boldsymbol{x})$ and $\psi_{c^+}(\boldsymbol{x})$ are their respective reconstructions of the variable ψ.

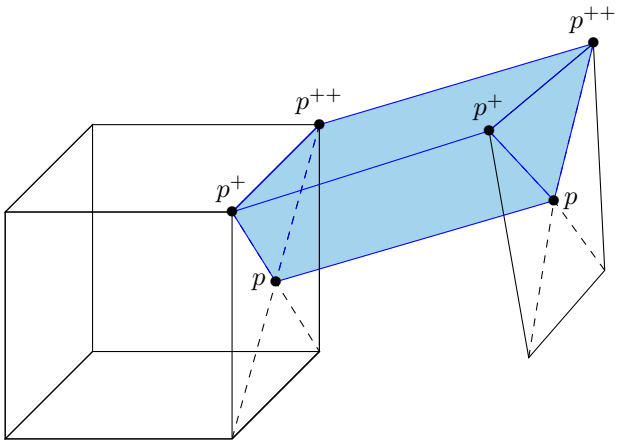

Figure 1: Representation of the swept region in blue, starting from an old triangle (formed by the points $\{p, p^+, p^{++}\}$) to the new one.

Piecewise-linear reconstructions of the variables on the Lagrangian grid are considered. In this case the reconstructed solution is expressed as

$$\tilde{\psi}_c(\boldsymbol{x}) = \psi_c + (\boldsymbol{\nabla}\psi)_c \cdot (\boldsymbol{x} - \boldsymbol{x}_c)\,,$$

where ψ_c is the known mean value in cell c, and $(\boldsymbol{\nabla}\psi)_c$ denotes the gradient of ψ in the cell, computed using a least-squares approach. Finally, in order to enforce monotonicity of the reconstructed solution, a standard Barth-Jespersen slope limiter is applied [3]. In addition, a compressive limiter technique is employed to limit the numerical diffusion of the volume fraction between materials. This procedure is recalled in Appendix for completeness. Finally, to enforce discrete total energy conservation, a correction is applied to the material internal energies. This correction ensures the positivity of the internal energies (at first order) and is also detailed in Appendix. The complete multi-material Lagrange-remapping methodology is summarized in the flowchart presented in Figure 2.

5 Numerical test cases

In this section, we investigate the behavior and accuracy of the overall Lagrange-Remapping proposed method. These include both hypo-elastic and hyper-elastic materials undergoing complex interactions, large deformations and strong discontinuities. The objective is to evaluate the method's robustness and accuracy. The numerical results are compared against those obtained from the updated Lagrangian scheme, which serves as a benchmark. Particular attention is given to the role of the compressive limiter in controlling numerical diffusion.

5.1 1D Wilkins like problem (hypo-elastic test)

The first numerical test is inspired by the benchmark proposed by Wilkins [44]. It consists of simulating a flying aluminum plate impacting a stationary aluminum target. The material is modeled using a Mie-Grüneisen equation of state with parameters $\rho_0 = 2785$, $a_0 = 5328$, $\Gamma_0 = 2$, and $s = 1.338$. The elastic-plastic behavior is described by an incremental constitutive law with a shear modulus $\mu = 27.6 \cdot 10^9$ and a yield strength $Y_0 = 3 \cdot 10^8$. The computational domain is defined as $x \in [-4 \cdot 10^{-2}, 5 \cdot 10^{-2}]$ and discretized using a structured mesh of 200 cells. At the initial time $t = 0$, the moving plate occupies the interval $x \in [-10^{-2}, 5 \cdot 10^{-3}]$ and is assigned a uniform velocity of $V_0 = 800$ in the x-direction, while the target remains at rest. The initial pressure P_0 is uniform throughout the domain. Wall boundary conditions are imposed at both the left and right boundaries. The simulation is run until $t = 2.5 \cdot 10^{-6}$. For this test, the simulation is executed using a single CPU. The computational time required for the Lagrangian simulation is 0.69s, whereas the indirect Euler simulation requires 0.84s. Figures 3 present the density and velocity profiles along the x-axis. At the moment of impact, left- and right-propagating shock waves develop at the flyer-target interface. The density and velocity profiles at $t = 2.5 \cdot 10^{-6}$ computed on a mesh of 200 cells are displayed, where results obtained with the Lagrangian scheme are shown in solid red and those from the indirect Euler method in dashed green. It is observed that both methods yield almost identical results, with the curves nearly superimposed.

5.2 2D Taylor impact problem (hypo-elastic test)

This test case considers the impact of a two-dimensional aluminum projectile against a rigid wall [25]. It serves as the planar counterpart to the classical Taylor impact problem with a cylindrical rod. The projectile is initially a rectangular plate of length $L = 5$ and thickness $H = 1$. The aluminum material is modeled using the Mie-Grüneisen equation of state with the material parameters as in the previous Wilkins-like test. The Lagrangian computational domain is defined as $[x, y] \in [0, 5] \times [-0.5, 0.5]$, and the projectile is initialized with a horizontal velocity $V_x(t = 0) = -150$. Free boundary conditions are imposed on all boundaries except the left boundary, which is treated as a rigid wall. The simulation is run until $t = 5 \cdot 10^{-3}$. During the impact, the projectile's kinetic energy is fully converted into internal energy through plastic dissipation, and the projectile's length gradually decreases, approaching a final value of approximately $L_{\text{final}} = 4.62$ for the Lagrange simulation and $L_{\text{final}} = 4.63$ for the Euler simulation. For the indirect Eulerian simulation, the projectile dimensions are kept identical, but the computational domain is extended to $[x, y] \in [0, 5.5] \times [-1, 1]$ and initialized with a perfect gas of density, velocity, pressure, and adiabatic

index around the solid

$$(\rho, \boldsymbol{V}, p, \gamma) = (5, \mathbf{0}, 10^5, 1.4).$$

For this test, the simulation is executed using four CPU. The computational time required for the indirect Euler simulation is 298s. In Figures 4 and 5, the density and pressure profiles are shown for a mesh of 220×80 cells at time $t = 5 \cdot 10^{-3}$. The top panels display the results obtained with the reference Lagrangian scheme, while the bottom panels show the results from the Lagrange-Remap scheme (indirect Euler). Figure 6 presents the computational mesh of 220×80 cells used for the simulation, superimposed with the pressure profile at time $t = 5 \cdot 10^{-3}$. Figure 6 (bottom) also presents the contour corresponding to a volume fraction of $\alpha^1 = 0.5$, superimposed on the final pressure distribution. It is observed that the final density and pressure profiles are very similar to the reference Lagrangian results (the same scale is used for both figures). As expected, the Lagrangian mesh is deformed at the final time, whereas the indirect Eulerian mesh remains unchanged. Moreover, the diffusion of material interfaces is controlled. Here, the compressive limiter plays a crucial role, effectively minimizing the natural smearing of material interfaces.

5.3 1D pile driving (hyper-elastic test)

This test case is taken from [16] and simulates the propagation of a shock wave in a one-dimensional steel pile. The pile is modeled as a parallelepiped of length $L = 10$ with a unit square cross section $(x, y, z) \in [0, 10] \times [-0.5, 0.5] \times [-0.5, 0.5]$. The boundary at $x = 0$ is fixed by a wall condition enforcing zero velocity. The shock wave is generated by applying a stress boundary condition $\mathbb{T}^b$ at $x = L$, with the imposed value $T^b = \mathbb{T}^b_{xx} = -5 \cdot 10^7$. All other external faces of the pile are treated as free surfaces, such that $\mathbb{T}^b \mathbf{n} = 0$. The hyperelastic material parameters of the steel are given by Young modulus $E = 200 \cdot 10^9$, Poisson ratio $\nu = 0$, and initial density $\rho_0 = 8000$. The temporal evolution of the stress at the wall is monitored up to a final time of $t^f = 8 \cdot 10^{-3}$. The shock wave reaches the wall at $t = 2 \cdot 10^{-3}$, where the stress amplitude doubles to a maximum value of $T^{\max}_{xx} = -10^8$. Figure 7 shows the stress $\mathbb{T}_{xx}$ measured at the wall using a mesh of $100 \times 3 \times 3$ cells. For this test, the simulation is executed using a single CPU. The computational time required for the Lagrangian simulation is 24s, whereas the indirect Euler simulation requires 30s. This one-dimensional problem is run on a three-dimensional mesh to demonstrate that no spurious 3D motion is produced by the scheme. The numerical results obtained with the Lagrangian scheme are shown in solid red, while those from the indirect Euler method are plotted with dashed green lines. Both methods give almost identical results with the curves nearly superimposed.

5.4 3D oscillating beam (hyper-elastic test)

This test case, presented in [37] considers the oscillations of a three-dimensional plate with geometry

$$(x, y, z) \in [-0.03, 0.03] \times [-0.005, 0.005] \times [-0.005, 0.005],$$

centered at the origin of the computational domain. The plate is initially perturbed by the velocity field $\mathbf{V}_0 = (0, V_y(x), 0)$ where

$$V_y(x) = A\,\omega\Big[g_1\left(\sinh(kx) + \sin(kx)\right) + g_2\left(\cosh(kx) + \cos(kx)\right)\Big].$$

Denoting the plate length by $L = 0.06$ and its square cross-section by $l = 0.01$, one introduces $k = \Omega(x + L/2)$ and $\Omega = 78.834$ while the other constants are defined as

$$A = 4.3369 \cdot 10^{-5}, \quad \omega = 2.3597 \cdot 10^{5}, \quad g_1 = 56.6368, \quad g_2 = 57.6455.$$

The plate is composed of Beryllium, modeled as a hyper-elastic material with initial density $\rho_0 = 1845$, Young modulus $E = 3.1827 \cdot 10^{11}$, and Poisson ratio $\nu = 0.0539$. Symmetry boundary conditions are imposed on the faces normal to the z-axis, while all other faces are subject to free-surface conditions. The oscillations of the plate are simulated up to a final time $t_f = 3{\cdot}10^{-5}$. For the indirect Eulerian simulation, the beam dimensions are kept identical, but the computational domain is extended to $(x, y, z) \in [-0.035, 0.035] \times [-0.015, 0.015] \times [-0.005, 0.005]$, and filled with a perfect gas of density, velocity, pressure, and adiabatic index

$$(\rho, \boldsymbol{V}, p, \gamma) = (5, \mathbf{0}, 10^5, 1.4).$$

In Figures 8-9 and 10-11, the density and pressure profiles are shown for a mesh of $100{\times}10{\times}10$ cells for the Lagrangian simulation and $100{\times}40{\times}10$ cells for the indirect Euler simulation, at times $t = 8.4{\cdot}10^{-6}$ and $t = 2.16{\cdot}10^{-5}$, respectively. The top panels present the results obtained with the Lagrangian scheme, while the middle and bottom panels display the corresponding results from the indirect Euler (Lagrange-Remap) scheme. In the bottom panels, only the cells with density values exceeding 500 are displayed. As expected, the Lagrangian mesh exhibits a noticeable deformation of the beam during the oscillations. Finally, the vertical displacements of the z-axis with respect to time until final time $t = 3 \cdot 10^{-5}$ are displayed for the Lagrange (red curve) and Euler (green crosses) simulations in Figure 12. For this test, the simulation is executed using a four CPU. The computational time required for the indirect Euler simulation is 863s. Overall, both approaches yield very similar results in terms of density and pressure distributions, confirming the accuracy of the Lagrange-Remap scheme when compared to the reference Lagrangian simulation.

5.5 Collapse of a thick-walled cylindrical beryllium shell

This 2D test problem was originally introduced in [24]. It consists of simulating the collapse of a cylindrical beryllium shell subjected to an initial radially inward velocity field. During the collapse, the shell's initial kinetic energy is progressively converted into internal energy through plastic dissipation. The final configuration of the shell is characterized by its inner and outer stopping radii. While this test was studied within a Lagrangian framework in [26], the present study considers a larger cubic domain surrounding the cylindrical shell, filled with a perfect gas. The resulting configuration defines a multiphase problem, which is solved here using the Lagrange-Remapping strategy described in this work. The shell is modeled using a Mie-Grüneisen equation of state with parameters

$$\rho_0 = 1845 \text{ kg/m}^3, \quad a_0 = 12870 \text{ m/s}, \quad \Gamma_0 = 2, \quad s = 1.124.$$

The surrounding perfect gas is defined by the state variables

$$(\rho, \boldsymbol{V}, p, \gamma) = (5, \mathbf{0}, 10^5, 1.4).$$

The elastic-plastic behavior of the shell is described by an incremental constitutive law characterized by a shear modulus $\mu = 151.9 \cdot 10^9$ Pa and a yield strength $Y_0 = 330 \cdot 10^6$ Pa. The two-dimensional computational domain is given by

$$[-0.11,\, 0.11] \times [-0.11,\, 0.11].$$

The initial inner and outer radii of the shell are $R_i = 80 \cdot 10^{-3}$ m and $R_o = 100 \cdot 10^{-3}$ m, respectively. The domain is discretized using a uniform Cartesian grid of 160×160 cells. The initial conditions are the following

$$(P_0, \boldsymbol{V}_0) = \left(10^{-6} \text{ Pa},\, -V_0 \frac{r}{R_i}\, \boldsymbol{e}_r\right),$$

where V_0 denotes the magnitude of the initial radial velocity and $r = \sqrt{x^2 + y^2}$ is the radial coordinate of a point with Cartesian coordinates (x, y). For $V_0 = 417.1$ m/s, Howell and Ball [24] reported inner and outer stopping radii of $R_i = 50 \cdot 10^{-3}$ m and $R_o = 78.1 \cdot 10^{-3}$ m. In Figure 13, the density distribution at the final time $t = 130 \cdot 10^{-6}$ s is shown (left), along with the computational mesh (right). The numerically obtained stopping radii are approximately $R_i = 51 \cdot 10^{-3}$ m and $R_o = 79 \cdot 10^{-3}$ m. The simulation is executed using four CPU. The computational time required is 429s. These results demonstrate very good agreement between the reference solution and the numerical results obtained using the indirect Euler approach.

5.6 Aluminium ball impact

This two-dimensional test case considers the impact of an aluminium ball onto a rectangular aluminium target, both embedded in a surrounding inviscid fluid. The aluminium is modeled using a Mie-Grüneisen equation of state, while the surrounding medium is described by a perfect gas equation of state. The computational domain $[-0.005, -0.0015] \times [-0.0025, 0.0025]$ is discretized into 150×200 control volumes. The first phase, representing the aluminium material (both the ball and the rectangular target), is defined through the volume fraction field

$$\alpha^1(x,y) = \begin{cases} 1, & \text{if } \left((x-x_0)^2 + (y-y_0)^2 \leq R^2\right) \\ & \quad \text{or } \left(x_{\min} \leq x \leq x_{\max} \text{ and } y_{\min} \leq y \leq y_{\max}\right), \\ 0, & \text{otherwise.} \end{cases}$$

For this simulation, we set $R = 5 \cdot 10^{-4}$, $x_0 = -4 \cdot 10^{-3}$ and $y_0 = 0$. The aluminium is described by a Mie-Grüneisen equation of state with parameters $\rho_0 = 2785$, $a_0 = 5328$, $\Gamma_0 = 2$, and $s = 1.338$. The initial density and pressure of the aluminium are set to $\rho_0 = 2785$ and $p_0 = 10^5$, respectively. Its elastic-plastic response is modeled using an incremental constitutive law with shear modulus $\mu = 27.6 \cdot 10^9$ and initial yield strength $Y_0 = 3 \cdot 10^8$. The surrounding gas is initialized as a perfect gas with state variables

$$(\rho, \boldsymbol{V}, p, \gamma) = (10^{-5}, \boldsymbol{0}, 10^{-5}, 1.4).$$

The initial velocity field is prescribed as

$$\boldsymbol{V}(x,y) = \begin{cases} V_0\, \boldsymbol{e}_x, & \text{if } (x-x_0)^2 + (y-y_0)^2 \leq R^2, \\ \boldsymbol{0}, & \text{otherwise,} \end{cases}$$

with $V_0 = 10^3$. Figure 14 displays the density field at successive times: $t = 0$, $t = 0.5{\cdot}10^{-6}$, $t = 1.0{\cdot}10^{-6}$, $t = 1.5{\cdot}10^{-6}$, $t = 2.0{\cdot}10^{-6}$, and $t = 2.5{\cdot}10^{-6}$. The simulation is executed using four CPU. The computational time required is 458s. These results show the capability of the numerical method to handle strongly coupled multi-material interactions between a compressible solid and a fluid. It evaluates the accuracy of interface capturing, the resolution of shock waves generated by the impact, and the robustness of the method in the presence of large material contrasts.

6 Conclusion

In this work, a Lagrange-Remap diffuse interface strategy has been presented for multi-material fluid-solid simulations. The deviatoric stress tensor (in the case of hypo-elastic materials) and the left Cauchy-Green tensor

(for isotropic hyper-elastic materials) are remapped componentwise using a face-sweeping procedure. The introduction of compressive limiters significantly mitigates the numerical smearing typically observed at the material interfaces, enabling accurate and robust multi-material simulations. A key advantage of the proposed approach lies in its simplicity, particularly when applied to fluid-solid interactions. The test cases considered, involving both solid and fluid materials, demonstrate that the Lagrange-Remap strategy produces results in close agreement with those obtained using a reference Lagrangian scheme. Future work will focus on extending this framework to the ALE-AMR strategy presented in [10, 11, 7], as well as on performing detailed comparisons with classical Volume-of-Fluid (VOF) and Moment-of-Fluid (MOF) interface reconstruction techniques. It should be noted, however, that the development of methods based on the MOF strategy remains challenging in three dimensions.

This work is supported by the U.S. Department of Energy (DOE), Office of Science, Fusion Energy Sciences, under Award No. DE-SC0024863: IFE-STAR.

References

[1] B. Després and F. Lagoutière. Contact discontinuity capturing schemes for linear advection and compressible gas dynamics. *J. Sci. Comp.*, 16:479–524, 2001.

[2] Andrew J. Barlow, Pierre-Henri Maire, William J. Rider, Robert N. Rieben, and Mikhail J. Shashkov. Arbitrary lagrangian–eulerian methods for modeling high-speed compressible multimaterial flows. *J. Comput. Phys.*, 322:603–665, 2016.

[3] T.J. Barth and D.C. Jespersen. The design and application of upwind schemes on unstructured meshes. *AIAA Paper, 27th Aerospace Sciences Meeting, Reno, Nevada*, 89-0366, 1989.

[4] D.J. Benson. Computational methods in Lagrangian and Eulerian hydrocodes. *Comput. Methods Appl. Mech. Eng.*, 99:235–394, 1992.

[5] J. Breil. *Numerical methods for Lagrangian and Arbitrary-Lagrangian-Eulerian Hydrodynamic Contribution to the simulation of High-Energy-Density-Physics Problems.* Habilitation à diriger des recherches, Bordeaux University, https://hal.science/tel-01467157., 2016.

[6] J. Breil, G. Georges, and P.-H. Maire. 3D cell-centered Lagrangian second order scheme for the numerical modeling of hyperelasticity system. *Comput. and Fluids*, 207:104523, 2020.

[7] Jérôme Breil, Guillaume Damour, Sébastien Guisset, and Arnaud Colaïtis. 3D mesh regularization within an ALE code using a weighted line sweeping method. *Comput. and Fluids*, 292:106591, 2025.

[8] D.E. Burton, T.C. Carney, N.R. Morgan, S.K. Sambasivan, and M.A. Kena-mond. A cell-centered lagrangian godunov-like method for solid dynamics. *Comput. and Fluids*, 229(83):33–47, 2013.

[9] V. Chiravalle, A. Barlow, and N.R. Morgan. 3D Cell-centered hydrodynamics with subscale closure model and multi-material remap. *Comput. and Fluids*, 207:104592, 2020.

[10] A. Colaïtis, S. Guisset, and J. Breil. A Cell-Centered AMR-ALE framework for 3d Multi-Material Hydrodynamics. Part I: Lagrangian and Indirect Euler AMR algorithms. *Submitted for publication and available at https://ssrn.com/abstract=5167115.*

[11] A. Colaïtis, S. Guisset, and J. Breil. A Cell-Centered AMR-ALE framework for 3d Multi-Material Hydrodynamics. Part II: linesweep ALE rezoning for nonconformal block-structured AMR meshes. *Submitted for publication and available at https://ssrn.com/abstract=5167116.*

[12] R. DeBar. Fundamentals of the KRAKEN code. *Technical Report UCIR-760*, 1974.

[13] B. Després and C. Mazeran. Lagrangian gas dynamics in dimension two and Lagrangian systems. *Arch. Ration. Mech. Anal.*, 178:327–372, 2005.

[14] M.M. Francois, M.J. Shashkov, T.O. Masser, and E.D. Dendy. A comparative study of multimaterial lagrangian and eulerian methods with pressure relaxation. *Comput. and Fluids*, 83:126–136, 2013.

[15] M.B. Friess and S. Kokh. An anti-diffusive lagrange-remap scheme for multi-material compressible flows with an arbitrary number of components. *ESAIM Proceedings*, 35:203–209, 2012.

[16] G. Gabriel. *Développement d'un schéma aux volumes finis centré lagrangien pour la résolution 3D des équations de l'hydrodynamique et de l'hyperélasticité.* PhD thesis, Université de Bordeaux, 2016.

[17] G. Georges, J. Breil, and P.-H. Maire. A 3D GCL compatible cell-centered Lagrangian scheme for solving gas dynamics equations. *J. Comput. Phys.*, 305:921–941, 2016.

[18] S.K. Godunov and E.I. Romenski. Nonstationary equations of nonlinear elasticity theory in eulerian coordinates. *Journal of Applied Mechanics and Technical Physics*, 13:868–884, 1972.

[19] S.K. Godunov, A. Zabrodine, M. Ivanov, A. Kraiko, and G. Prokopov. Résolution numérique des problèmes multi-dimensionnels de la dynamique des gaz. *Éditions Mir Moscou*, 1979.

[20] S. Guisset, G. Damour, and J. Breil. Cell-centered indirect Arbitrary Lagrangian-Eulerian numerical strategy for solving 3D gas dynamics equations. *J. Comput. Phys.*, 505:112903, 2024.

[21] S. Guisset, S. Peluchon, A. Colaïtis, and J. Breil. A 3D multi-material cell-centered indirect Arbitrary Lagrangian-Eulerian scheme using compressive limiters. *To appear in Commun. Comput. Phys. Available at https://ssrn.com/abstract=5412394.*

[22] E. Gurtin, E. Fried, and L. Anand. *The Mechanics and Thermodynamics of Continua.* Cambridge University Press, 2010.

[23] G.A. Holzapfel. *Nonlinear Solid Mechanics: A Continuum Approach for Engineering.* John Wiley & Sons, 2000.

[24] B.P. Howell and G.J. Ball. A free-lagrange augmented godunov method for the simulation of elastic-plastic solids. *J. Comput. Phys*, 175:128–167, 2002.

[25] G. Kluth and B. Després. Discretization of hyperelasticity on unstructured mesh with a cell-centered lagrangian scheme. *J. Comput. Phys.*, 229(24):9092–9118, 2010.

[26] P.-H. Maire, R. Abgrall, J. Breil, R. Loubère, and B. Rebourcet. A nominally second-order cell-centered lagrangian scheme for simulating elastic–plastic flows on two-dimensional unstructured grids. *J. Comput. Phys.*, 235:626–665, 2013.

[27] P.-H. Maire, R. Abgrall, J. Breil, and J. Ovadia. A cell-centered Lagrangian scheme for two-dimensional compressible flows problems. *SIAM J. Sci. Comput.*, 29:1781–1824, 2007.

[28] V. Maltsev, M. Skote, and P. Tsoutsanis. High-order methods for diffuse-interface models in compressible multi-medium flows: A review. *Physics of Fluids*, 34(2):021301, 2022.

[29] L.E. Malvern. Introduction to the mechanics of a continuous medium. *Englewood Cliffs*, 1969.

[30] B. Manach-Pérennou, R. Chauvin, S. Guisset, and A. Llor. Cell-centered Lagrangian scheme for multi-material flows with pressure equilibration. *Comput. and Fluids*, 250:105705, 2023.

[31] L.G. Margolin and M. Shashkov. Second-order sign-preserving remapping on general grids. *J. Comput. Phys.*, 184:266–298, 2003.

[32] R. Menikoff and B.J. Plohr. The riemann problem for fluid flow of real materials. *Rev. Mod. Phys.*, 61:75–130, 1989.

[33] R. W. Ogden. *Non-linear elastic deformations*. Courier Corporation, 1997.

[34] L. Qian, D.M Causon, C.G. Mingham, and D.M. Ingram. A free-surface capturing method for two fluid flows with moving bodies. *Proc. R. Soc. A.*, 462(2065):21–42, 2006.

[35] S. Jaouen and F. Lagoutière. Numerical transport of an arbitrary number of components. *Comput. Methods Appl. Mech. Eng.*, 196(33-34):3127–3140, 2007.

[36] S. Kokh and F. Lagoutière. An anti-diffusive numerical scheme for the simulation of interfaces between compressible fluids by means of a five-equation model. *J. Comput. Phys.*, 229(8):2773–2809, 2010.

[37] S.K. Sambasivan, M.J. Shashkov, and D.E. Burton. A finite volume cell-centered lagrangian hydrodynamics approach for solids in general unstructured grids. *Int. J. Numer. Meth. Fluids*, 72:770–810, 2013.

[38] R. Saurel and C. Pantano. Diffuse-interface capturing methods for compressible two-phase flows. *Annual Review of Fluid Mechanics*, 50:105–130, 2018.

[39] J.C. Simó and T.J.R. Hughes. Computational inelasticity. interdisciplinary applied math- ematics: Mechanics and materials. *Springer*, 1998.

[40] C.A. Swenson. Volume dependence of the grüneisen parameter: Alkali metals and nacl. *Phys. Rev. B*, 31(2):1150–1153, 1985.

[41] L. Tallois, S. Peluchon, and P. Villedieu. A second-order extension of a robust implicit-explicit acoustic-transport splitting scheme for two-phase flows. *Comput. and Fluids*, 244:105531, 2022.

[42] C. Truesdell and W. Noll. *The Non-Linear Field Theories of Mechanics*. Springer, 1965.

[43] F. De Vuyst, T. Gasc, R. Motte, M. Peybernes, and R. Poncet. Lagrange-flux eulerian schemes for compressible multimaterial flows. *Proc. of the ECCOMAS Congress 2016, VII Eur. Congress on Comp. Meth. in Appl. Sci. and Eng., Crete Island, Greece, pp. 1165–1178 (2016).*

[44] M.L. Wilkins. Calculation of elastic plastic flow. *Methods Comput. Phys.*, 3:211–263, 1964.

[45] D. Zuzio, J.-L. Estivalezes, P. Villedieu, and G. Blanchard. Numerical simulation of primary and secondary atomization. *Comptes Rendus Mécanique*, 341(1):15–25, 2013.

A Diffuse interfaces and compressive limiters

In the present work, material interfaces are modeled as diffuse transition regions, where different materials may numerically mix. Such methods are commonly referred to as diffuse interface methods. These approaches have become increasingly popular, since the artificial smearing of interfaces can be significantly reduced by employing anti-diffusive techniques [1, 35, 36]. This appendix is devoted to an anti-diffusive strategy based on the use of compressive limiters. When linear reconstructions are employed, overly steep gradients may introduce non-physical extrema, leading to spurious oscillations that threaten the stability of the numerical scheme. To prevent this issue, a monotonicity criterion is enforced through the application of a slope limiter, which rescales the reconstructed gradient. Specifically, the gradient is multiplied by a scalar coefficient $\kappa_c \in [0,1]$, ensuring that the reconstructed values remain bounded by the neighboring cell averages. The corresponding limited reconstruction can be expressed as

$$\psi_c^{lim}(\boldsymbol{x}) = \psi_c + \kappa_c \left(\boldsymbol{\nabla}\psi\right)_c \cdot (\boldsymbol{x} - \boldsymbol{x}_c)\,,$$

with

$$\psi_c^{min} \leq \psi_c^{lim}(\boldsymbol{x}) \leq \psi_c^{max}, \quad \boldsymbol{x} \in \omega_c, \tag{5}$$

where $\psi_c^{\min}$ and $\psi_c^{\max}$ denote, respectively, the minimum and maximum values of the scalar field ψ within the neighborhood of cell c. In this work, the neighborhood is defined using a face-based stencil around c. Since a linear reconstruction is employed, the extremal values of the reconstructed field are necessarily attained at the cell boundaries, i.e., at the cell vertices

$$\psi_c^{min} \leq \psi_c^{lim}(\boldsymbol{x}_p) \leq \psi_c^{max}, \quad \boldsymbol{x} \in \omega_c,$$

The computation of the limiting coefficient now needs to be specified. The monotonicity criterion (5) naturally leads to the well-known Barth-Jespersen limiter [3]. In this formulation, the limiter coefficient κ_c is defined as

$$\kappa_c = \min_{p \in \mathcal{P}(c)} \left(\kappa_{c,p}\right),$$

where

$$\kappa_{c,p} = \begin{cases} \min\left(\dfrac{\psi_c^{max} - \psi_c}{\tilde{\psi}_c(\boldsymbol{x}_p) - \psi_c}, 1\right) & \text{if} \quad \tilde{\psi}_c(\boldsymbol{x}_p) > \psi_c, \\ \min\left(\dfrac{\psi_c^{min} - \psi_c}{\tilde{\psi}_c(\boldsymbol{x}_p) - \psi_c}, 1\right) & \text{if} \quad \tilde{\psi}_c(\boldsymbol{x}_p) < \psi_c, \\ 1 & \text{if} \quad \tilde{\psi}_c(\boldsymbol{x}_p) = \psi_c, \end{cases}$$

This limiting strategy is applied to all remapped quantities except for the material volume fraction. During the remapping step, the volume fraction tends to diffuse, which can smear the interfaces between different materials. Following the approach of [41], we employ a compressive limiter exclusively for the remapping of the material volume fraction to sharpen the representation of these discontinuities. The method consists of modifying the Barth-Jespersen limiter to steepen the initially piecewise-constant volume fraction field. While the original limiter enforces that the reconstruction remains within the local extrema of neighboring cells and ensures linear exactness through $\kappa_{c,p} \leq 1$, capturing sharp discontinuities requires a compressive adjustment. In this case, the only constraint is the satisfaction of the local maximum principle. Accordingly, following [41, 34, 45], we relax the linear-preservation requirement and redefine $\kappa_{c,p}$ by introducing a parameter $\beta \in [1, +\infty[$ to control the compressiveness of the limiter

$$\kappa_{c,p} = \begin{cases} \min\left(\dfrac{\psi_c^{max} - \psi_c}{\tilde{\psi}_c(\boldsymbol{x}_p) - \psi_c}, \beta\right) & \text{if} \quad \tilde{\psi}_c(\boldsymbol{x}_p) > \psi_c, \\ \min\left(\dfrac{\psi_c^{min} - \psi_c}{\tilde{\psi}_c(\boldsymbol{x}_p) - \psi_c}, \beta\right) & \text{if} \quad \tilde{\psi}_c(\boldsymbol{x}_p) < \psi_c, \\ \beta & \text{if} \quad \tilde{\psi}_c(\boldsymbol{x}_p) = \psi_c, \end{cases}$$

In practice, the compressive limiter is set to $\beta = 2$ for all material volume fractions, while the classical limiter with $\beta = 1$ is applied to the other remapped variables. The choice $\beta = 2$ corresponds to the maximum theoretical value of the compressive limiter on a Cartesian grid [41]; larger values do not enhance its compressive effect. In fact, similar results are observed if a higher value of β is used. This modification of the standard limiter is straightforward to implement, requiring minimal adjustments, and the remapping procedure remains identical for both pure and mixed cells.

B Enforcing total discrete energy conservation

The remapping procedure presented here guarantees that both the total momentum and the material internal energies are updated consistently. Remapped quantities are denoted with a tilde symbol

$$\sum_c (m\boldsymbol{V})_c = \sum_{\tilde{c}} (m\boldsymbol{V})_{\tilde{c}}, \qquad \sum_c \left(m^k \varepsilon^k\right)_c = \sum_{\tilde{c}} \left(m^k \varepsilon^k\right)_{\tilde{c}}.$$

However, it should be noted that, since the squared velocity $\boldsymbol{V}^2$ is not remapped, the total kinetic energy of the domain may vary during the remapping step

$$\sum_{\tilde{c}} \frac{1}{2} \left(m\boldsymbol{V}^2\right)_{\tilde{c}} \neq \sum_{\tilde{c}} \frac{1}{2} \frac{(m\boldsymbol{V})_{\tilde{c}}^2}{m_{\tilde{c}}}.$$

More precisely, the total kinetic energy after remapping generally differs from the kinetic energy computed using the remapped mass and momentum. This discrepancy has important implications, as it implies that discrete total energy conservation is not automatically satisfied. One possible approach is to follow the procedure proposed in [12] within the present cell-centered framework. A straightforward strategy would be to remap the total energy and then adjust the internal energy; however, this does not ensure that the internal energy remains positive. A more robust alternative is to explicitly remap the kinetic energy, defined as $m\boldsymbol{V}^2/2$, and then compute the difference between this remapped kinetic energy and the kinetic energy derived from the remapped mass and momentum. This difference can then be used to correct the remapped material internal energy in each cell as follows

$$\left(m^k\varepsilon^k\right)_{\tilde{c}}^{corrected} = (m^k\varepsilon^k)_{\tilde{c}} + \frac{m_{\tilde{c}}^k}{m_{\tilde{c}}}\left(\frac{1}{2}\left(m\boldsymbol{V}^2\right)_{\tilde{c}} - \frac{1}{2}\frac{(m\boldsymbol{V})_{\tilde{c}}^2}{m_{\tilde{c}}}\right).$$

It can easily be shown that these revised definitions of the material internal energies enforce discrete total energy conservation. Moreover, in the simplified case of a first-order remapping, it can be proven that the correction term remains positive [21].

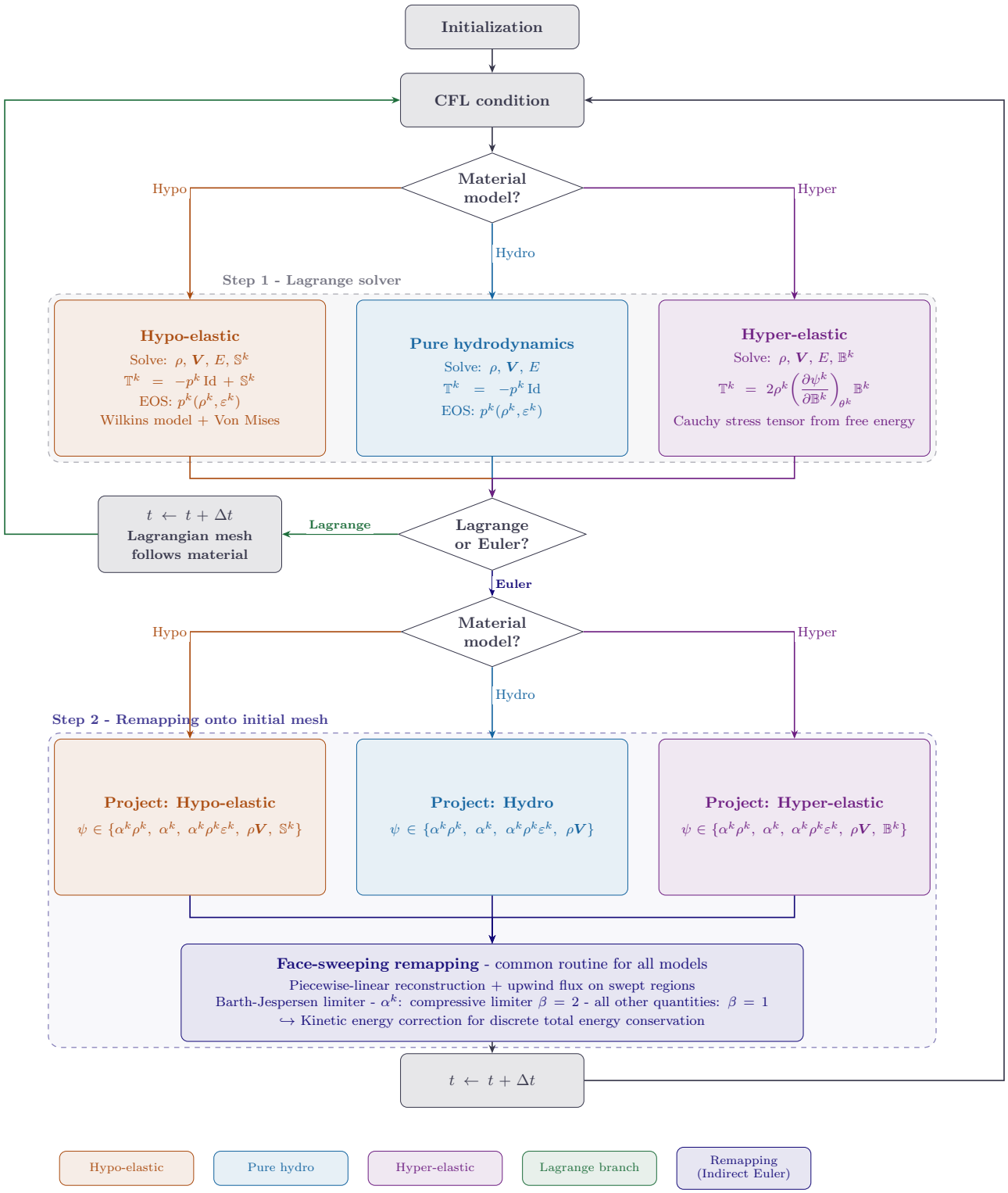

Figure 2: Flowchart of the multi-material Lagrange-remapping methodology.

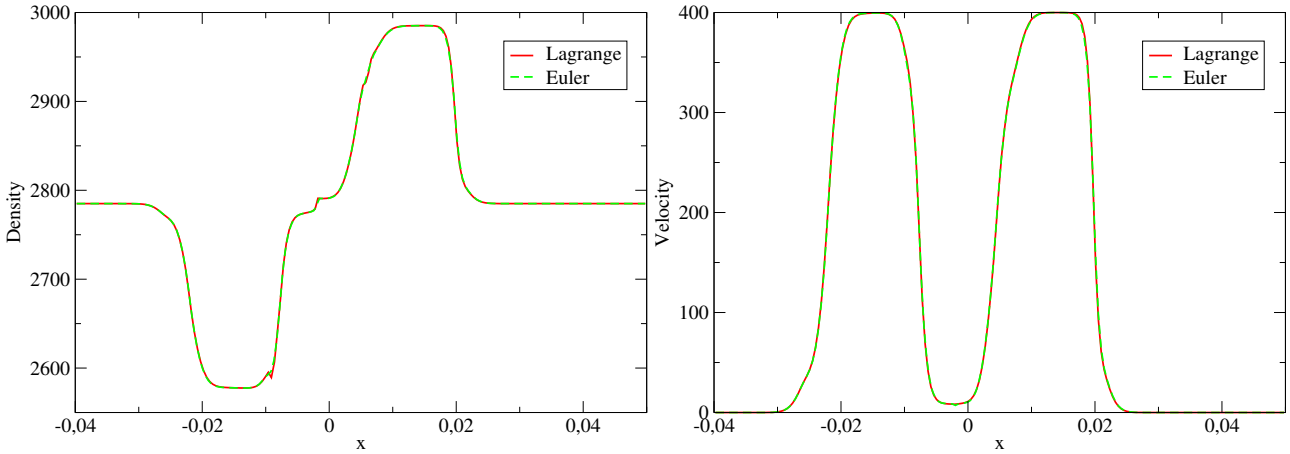

Figure 3: Density (left) and velocity (right) profiles at time $t = 2.5 \cdot 10^{-6}$, computed with a mesh of 200 cells. Results obtained with the Lagrangian scheme are shown in solid red, while those computed with the indirect Euler method are represented by dashed green curves.

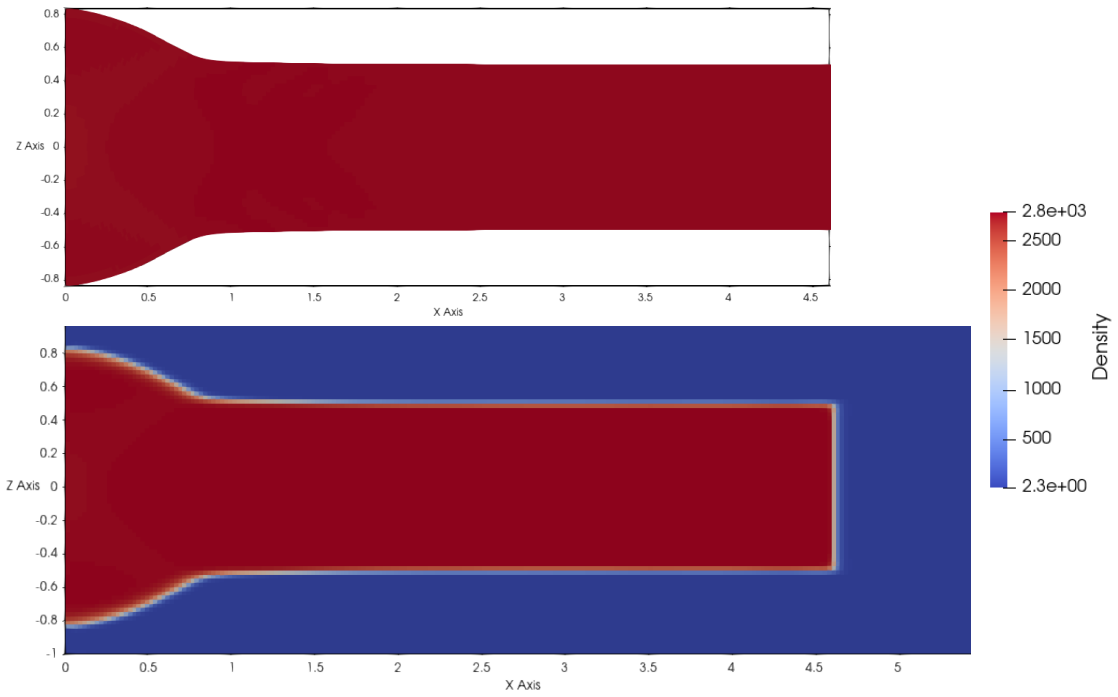

Figure 4: Density profile obtained on a 220×80 cells mesh at time $t = 5 \cdot 10^{-3}$. Top: results computed with the Lagrangian scheme. Bottom: results obtained with the Lagrange-Remap scheme (indirect Euler).

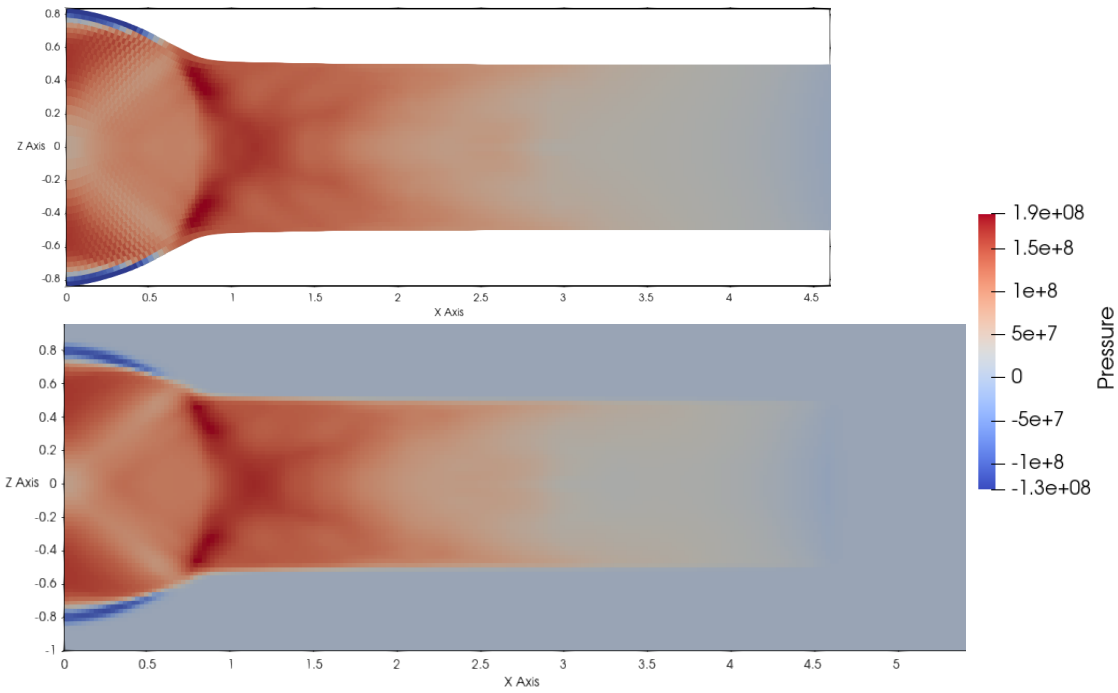

Figure 5: Pressure profile obtained on a 220×80 cells mesh at time $t = 5 \cdot 10^{-3}$. Top: results computed with the Lagrangian scheme. Bottom: results obtained with the Lagrange-Remap scheme (indirect Euler).

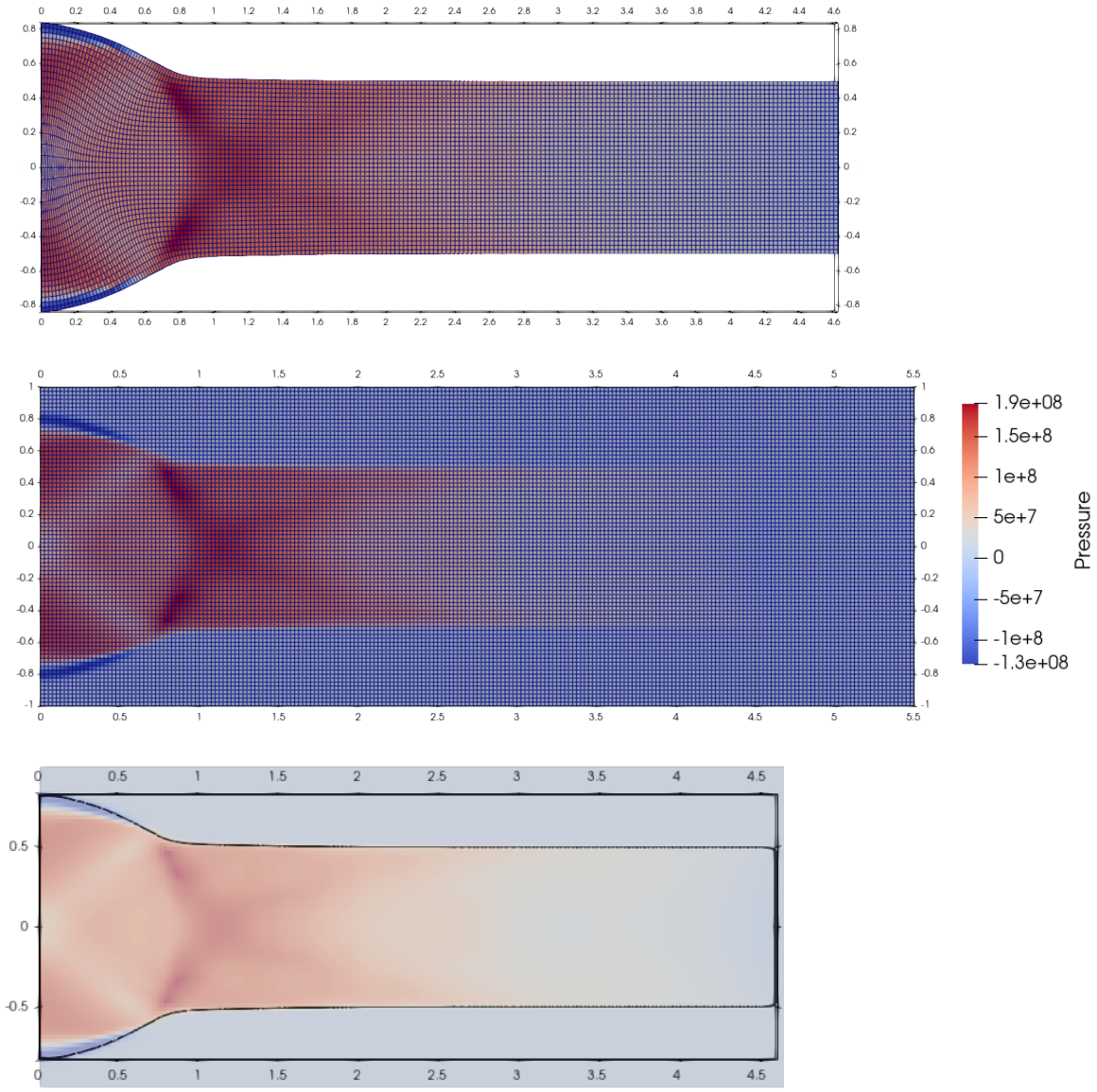

Figure 6: Computational mesh of 220×80 cells used for the simulation, superimposed with the pressure profile at time $t = 5{\cdot}10^{-3}$. Top: results from the Lagrangian scheme. Middle: results from the Lagrange-Remap scheme (indirect Euler). Bottom: contour level of the volume fraction ($\alpha^1 = 0.5$) displayed on top of the pressure distribution.

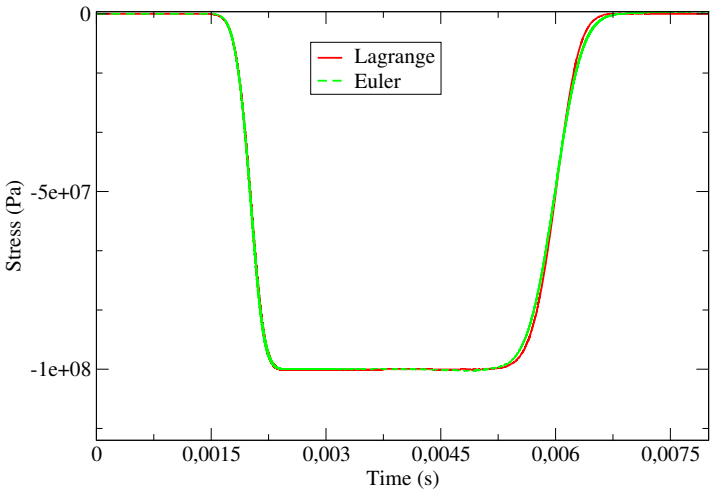

Figure 7: 1D pile driving. Stress profile $\mathbb{T}_{xx}$ obtained at the wall using a mesh of 100 cells. Results computed with the Lagrangian scheme are shown in solid red, while those from the indirect Euler scheme are displayed with dashed green lines.

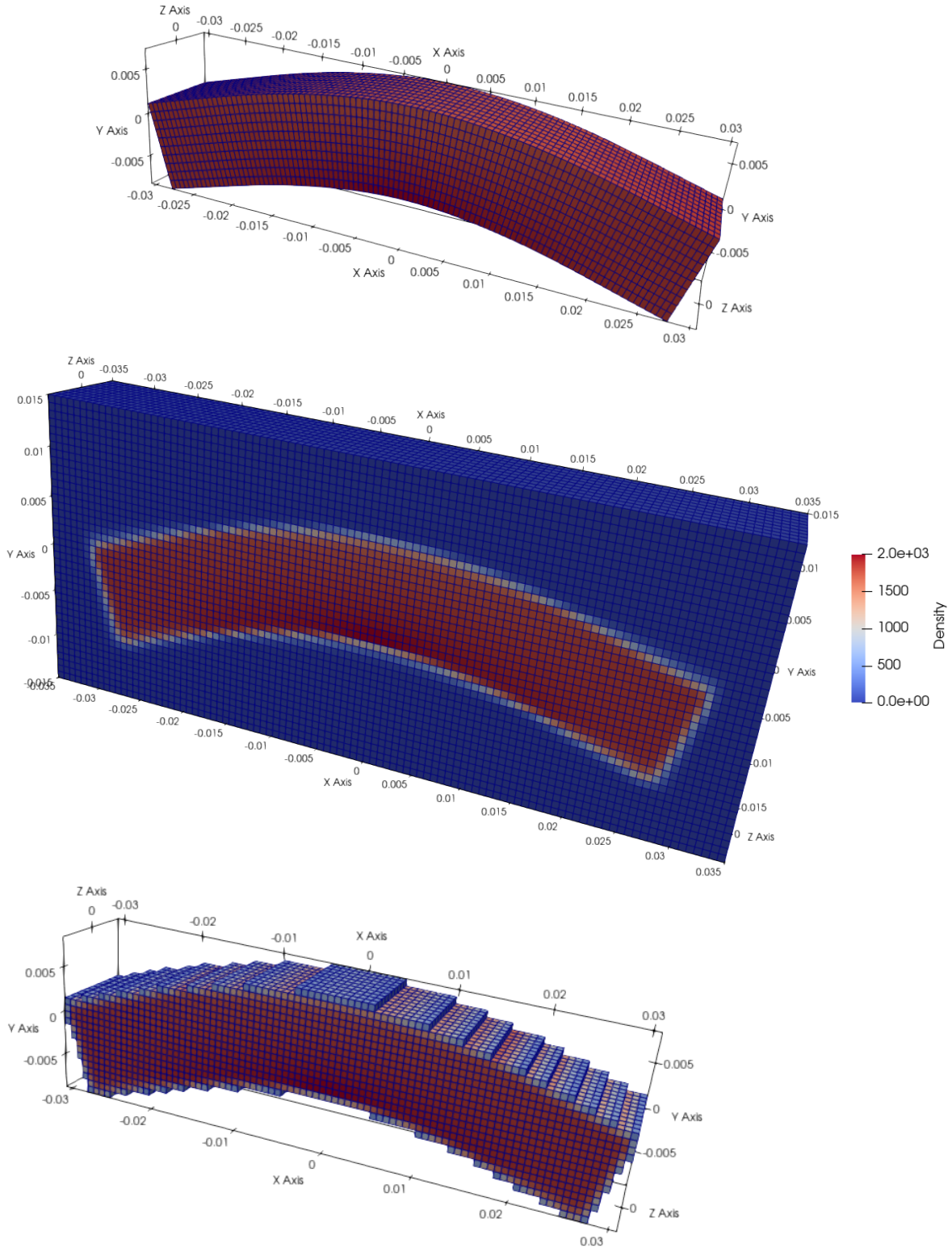

Figure 8: 3D oscillating beam. Density profile obtained with a mesh of $100 \times 10 \times 10$ cells for the Lagrangian simulation and $100 \times 40 \times 10$ cells for the indirect Euler simulation at time $t = 8.4 \cdot 10^{-6}$. Results from the Lagrangian scheme are shown in the top figure, while the middle and bottom figures correspond to the indirect Euler (Lagrange-Remap) scheme. The bottom figure displays only the cells where the density value exceeds 500.

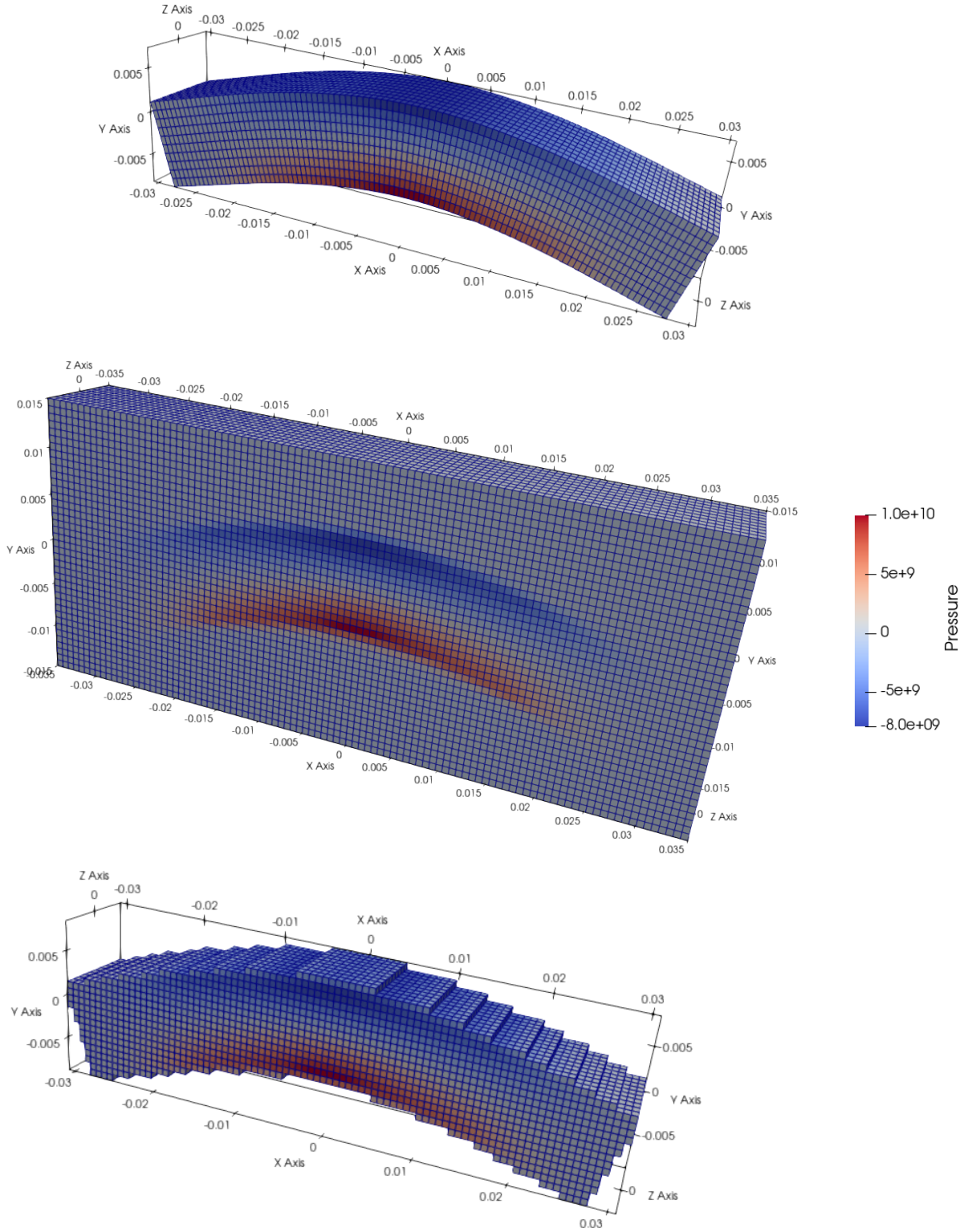

Figure 9: 3D oscillating beam. Pressure profile obtained with a mesh of $100 \times 10 \times 10$ cells for the Lagrangian simulation and $100 \times 40 \times 10$ cells for the indirect Euler simulation at time $t = 8.4 \cdot 10^{-6}$. Results from the Lagrangian scheme are shown in the top figure, while the middle and bottom figures correspond to the indirect Euler (Lagrange-Remap) scheme. The bottom figure displays the pressure profile but only in the cells where the density value exceeds 500.

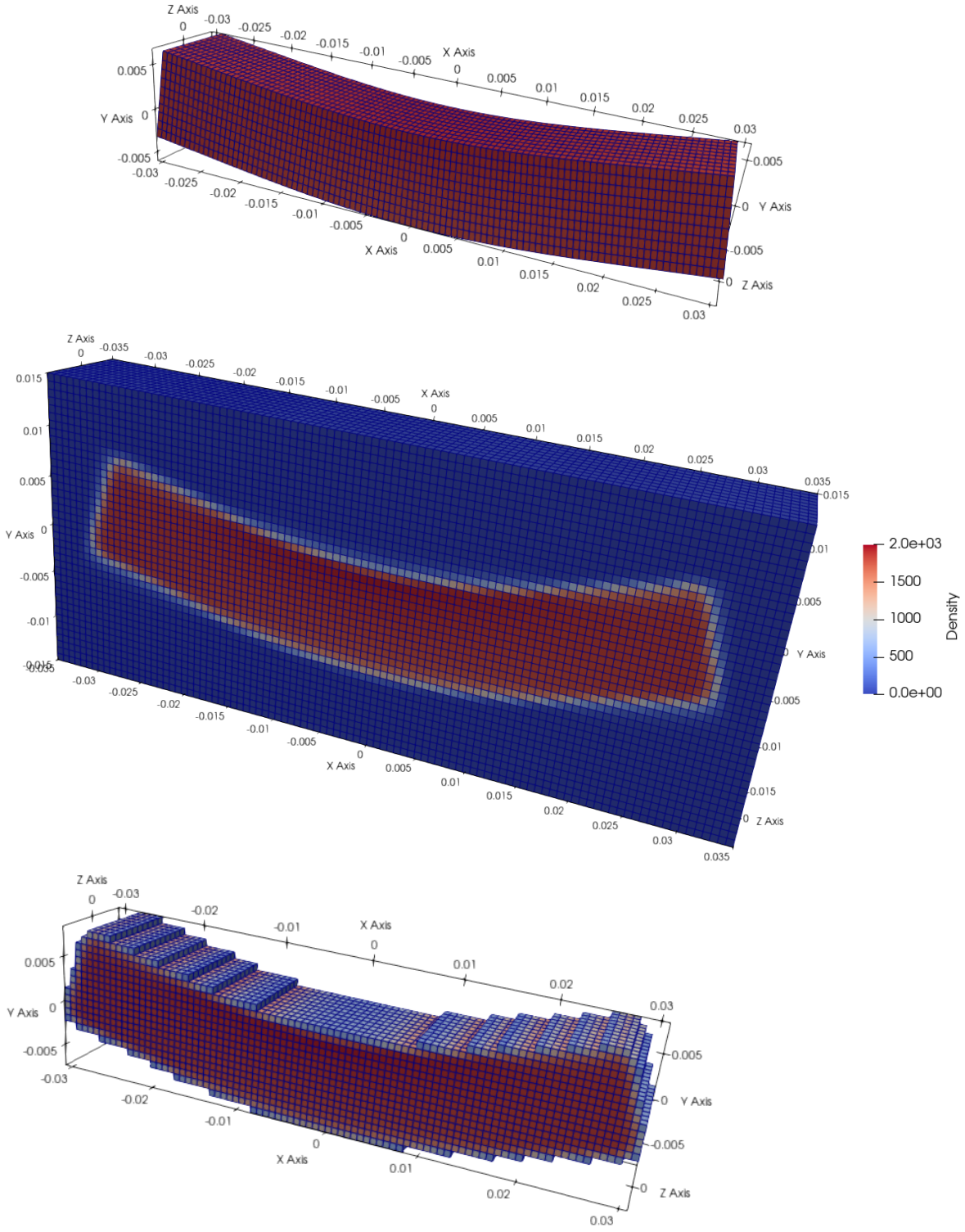

Figure 10: 3D oscillating beam. Density profile obtained with a mesh of $100 \times 10 \times 10$ cells for the Lagrangian simulation and $100 \times 40 \times 10$ cells for the indirect Euler simulation at time $t = 2.16 \cdot 10^{-5}$. Results from the Lagrangian scheme are shown in the top figure, while the middle and bottom figures correspond to the indirect Euler (Lagrange-Remap) scheme. The bottom figure displays only the cells where the density value exceeds 500.

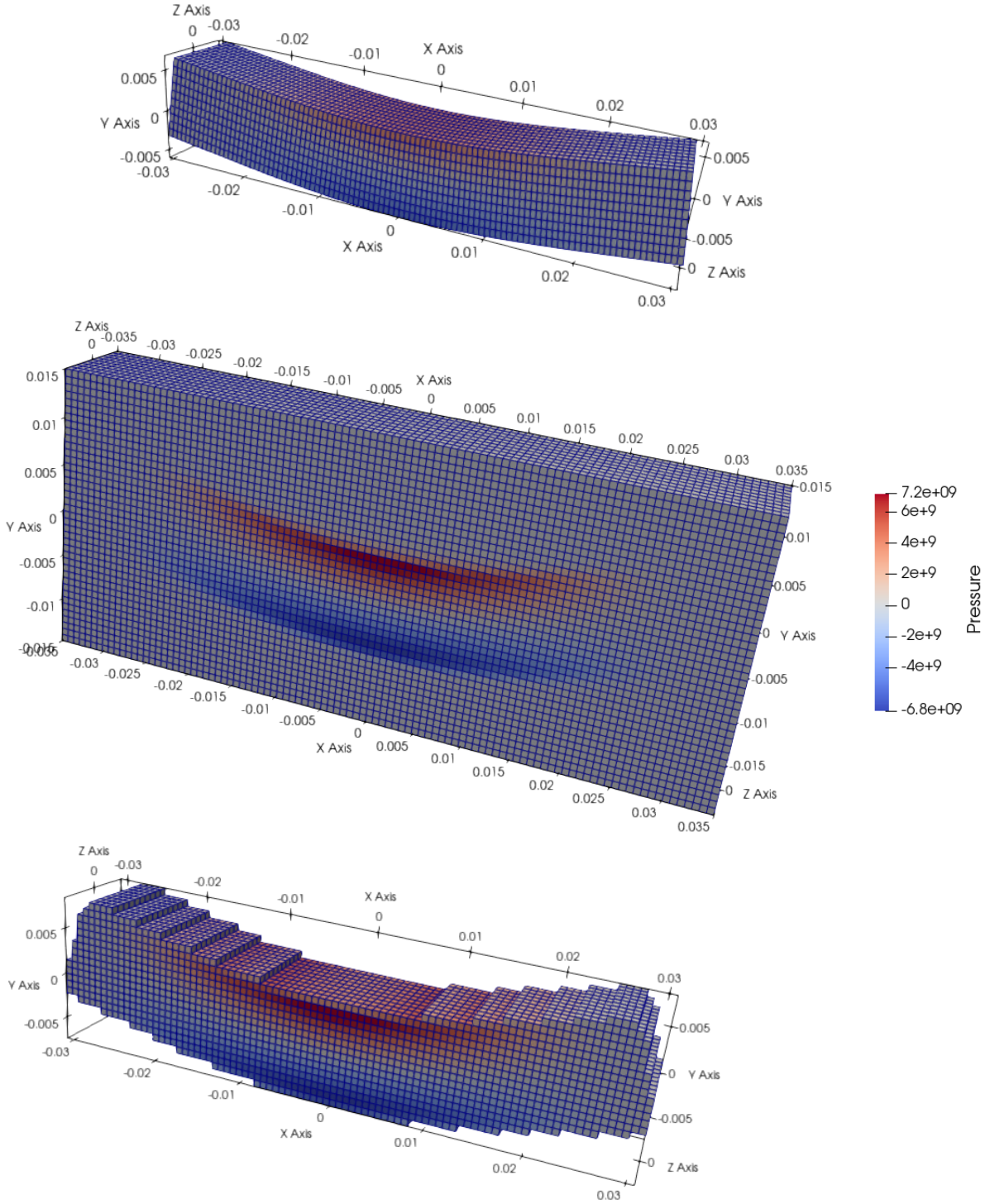

Figure 11: 3D oscillating beam. Pressure profile obtained with a mesh of $100 \times 10 \times 10$ cells for the Lagrangian simulation and $100 \times 40 \times 10$ cells for the indirect Euler simulation at time $t = 2.16 \cdot 10^{-5}$. Results from the Lagrangian scheme are shown in the top figure, while the middle and bottom figures correspond to the indirect Euler (Lagrange-Remap) scheme. The bottom figure displays the pressure profile but only in the cells where the density value exceeds 500.

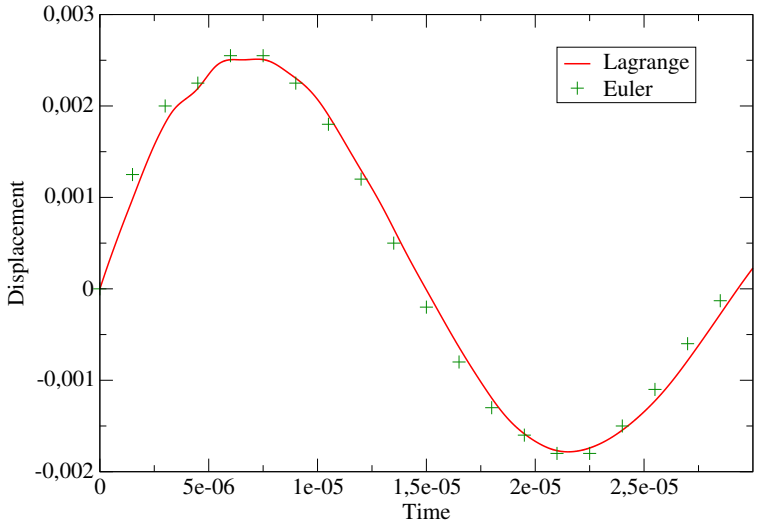

Figure 12: 3D oscillating beam. Vertical displacement of the z-axis with respect to time until final time $t = 3 \cdot 10^{-5}$ for Lagrange (red curve) and Euler (green crosses) simulations.

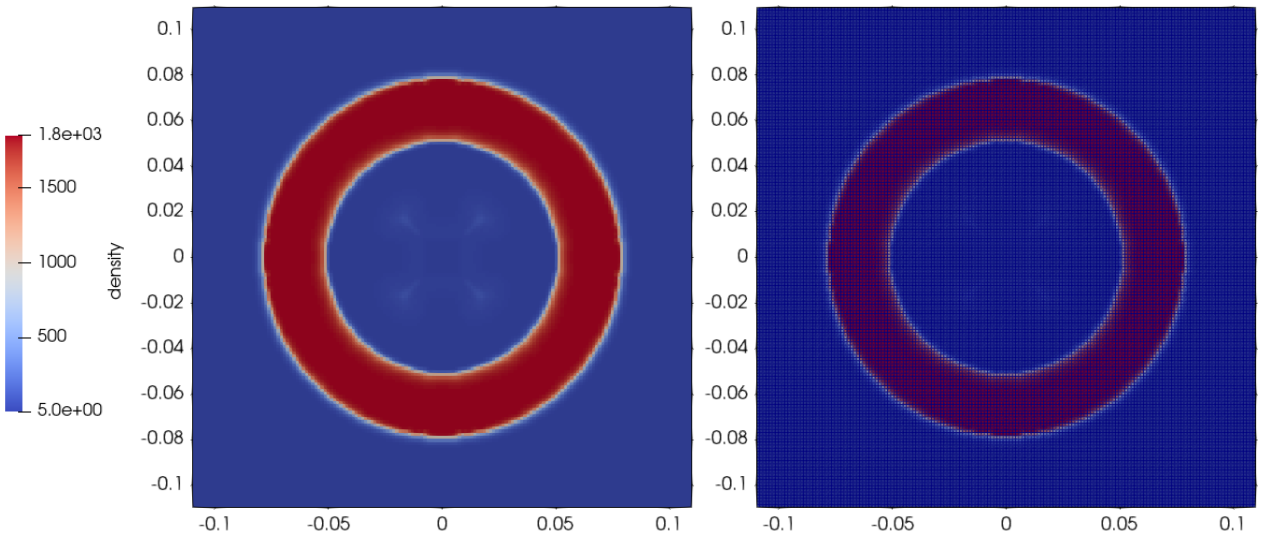

Figure 13: Beryllium shell. Density profile obtained at time $t = 130 \cdot 10^{-6}$ (indirect Euler simulation). The 160×160 mesh is displayed on the right picture.

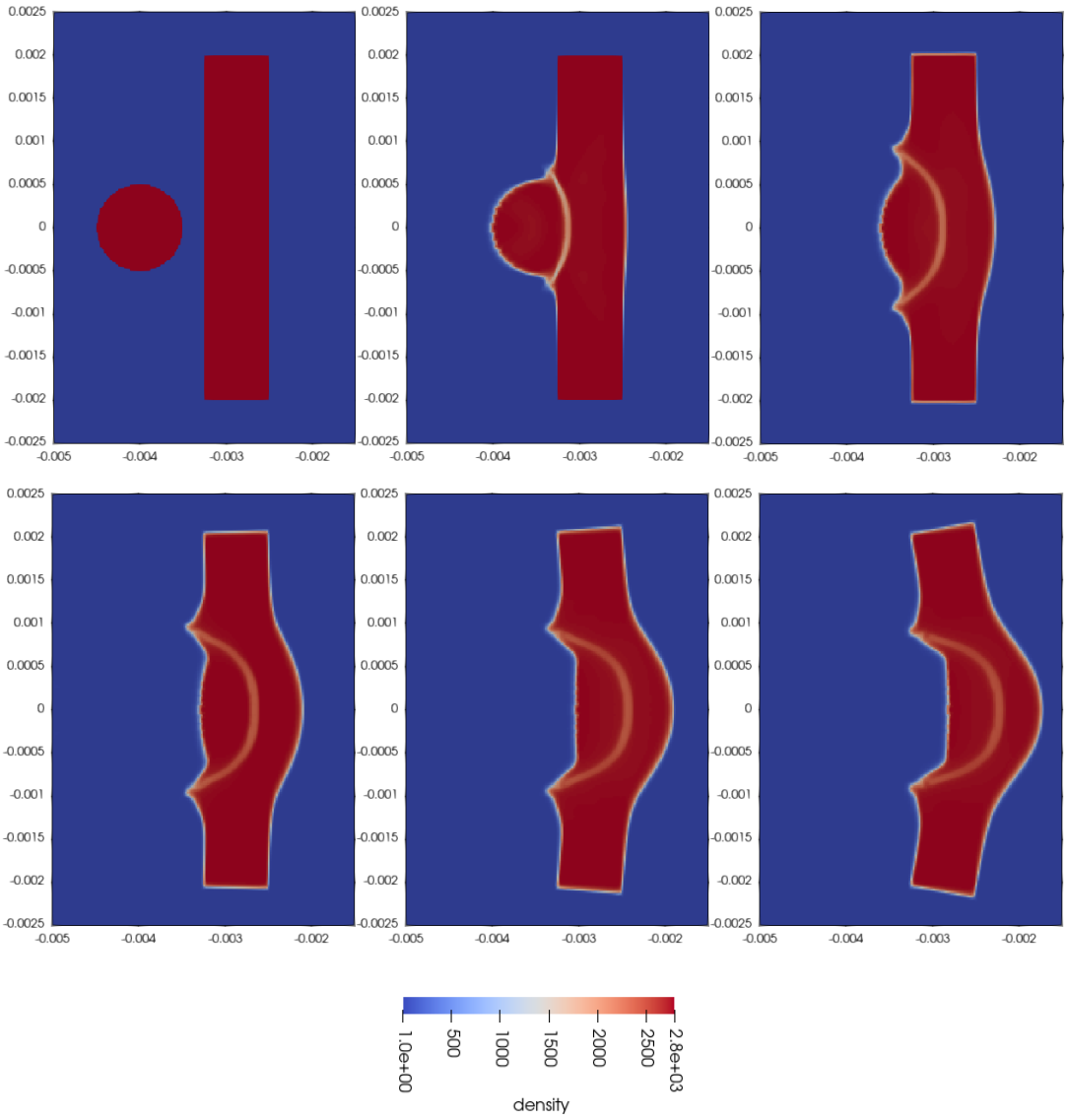

Figure 14: Aluminium ball impact. Density profile obtained at time $t = 0$ (top left), $t = 0.5 \cdot 10^{-6}$ (top middle), $t = 1.0 \cdot 10^{-6}$ (top right), $t = 1.5 \cdot 10^{-6}$ (bottom left), $t = 2.0 \cdot 10^{-6}$ (bottom middle), $t = 2.5 \cdot 10^{-6}$ (bottom right) (indirect Euler simulation).